Characterization and Thermodynamic Analysis of a Series of Mn^{III}-OH Complexes that undergo Hydrogen Atom Transfer Reactions

By

Aruna I. Munasinghe

Submitted to the Graduate Degree Program in Chemistry and the Graduate Faculty of University of Kansas in Partial Fulfillment of the Requirements for the Degree of Master of Science.

_____

Chairperson: Dr. Timothy Jackson

_____

Dr. Mikhail V. Barybin

_____

Dr. James D. Blakemore

Date Defended: October 25th, 2018

The Dissertation Committee for Aruna Indeewara Munasinghe certifies that this is the approved version of the following dissertation:

Characterization and Thermodynamic Analysis of a Series of Mn^{III}-OH Complexes that undergo Hydrogen Atom Transfer Reactions

_____

Chairperson: Dr. Timothy A. Jackson

Date Approved: 11/20/2018

Abstract

Mononuclear Mn^{III}-hydroxo motifs employ hydrogen atom transfer (HAT) reactions in biology and synthetic systems to oxidize a wide range of C–H or O–H bonds. Extensive studies on high valent Fe and Mn model systems exist, while studies on low and mid valent manganese complexes are less explored. In an effort to broaden the knowledge on structure and reactivity relationships of Mn^{III}-OH motifs in HAT reactivity, a novel Mn^{III}-OH complex is introduced to the $[Mn^{III}(OH)(dpaq^{R})](OTf)$ series.

Understanding the HAT reactivity of Mn^{III}–OH moieties in biological reactions rely on their reaction driving forces that are governed by the redox potential of the oxidant and the p*Ka* value of the proton abstractor. However determining these thermodynamic parameters for biological systems is difficult. Alternatively, an understanding about these parameters can be obtained by studying their corresponding synthetic model systems. In an effort to understand the HAT step of the Mn-lipoxygenase catalytic cycle, a series of $[Mn^{II}(OH_2)(dpaq^{R})]^{+}$ complexes were prepared.

Acknowledgments

First and foremost, I want to thank my research advisor, Professor Timothy Jackson. I cannot elaborate enough how helpful you have been as a mentor to me in research work and class room setting. I express my sincere gratitude for your contributions of time, ideas and funding invested in me and accepting me into your research group. The enthusiasm and vast knowledge that you have in the field of bioinorganic chemistry and your problem solving strategies have always inspired me to strive to work harder.

I would also like to thank my committee members, Professor Misha Barybin and Professor James Blakemore for agreeing to serve on my master's thesis committee. Both of you have been great faculty advisors to talk with. I am also grateful for serving as committee members in my Orals Comprehensive examination few months back.

There have been many others who have helped me to make my research successful at KU. I would like to thank Dr. Victor Day for all the help given in solving several crystal structures of Mn complexes. I want to express my gratitude to Dr. Justin Douglas, for helping me out and guiding me on NMR and EPR data acquisition/analysis. I also want to thank Sarah Neuenswander for helping me in running samples in the Siena NMR instrument and for long and helpful discussion on planning of experiments. I want to thank the Barybin Group for providing me an opportunity to do electrochemistry using their setup. Specifically, Jason Applegate and Nate Erickson, thank you for teaching and answering my question about Cyclic Voltammetry. Additionally, I would like to thank the University of Kansas for providing me this great opportunity.

I am deeply indebted to many of past and current Jackson group members. Hannah, thank you for being so helpful and encouraging to me throughout since I joined the group. I also like to thank Gayan and Derek for laying out a solid foundation of research knowledge on Mn-dpaq complexes which contributed to the success of my research. I also want to extend my appreciation to Derek for all the guidance and help given to my research work. Allyssa, thank you for being a helpful lab partner and I learnt a lot from you. Melissa, thank you for being a supportive person in and out of lab and it was fun sharing hood space with you. Josh, I want to thank you for teaching me a lot of lab procedures including how to work with the glove box and schlenk lines. Yuri, I want to express my gratitude to you for being such a good friend in the lab and I enjoyed working with you. Liz and Jaycee, I am glad that you guys joined the group and I wish you two a successful graduate life.

Lastly, I want to express my gratitude to my loving parents and little brother. You have always been an inspiration to me and have supported me throughout my life which I am very much thankful of. I cannot emphasize enough how much your caring and love have supported me in life, especially when times are difficult. I must also thank Sachini, for being such a kind and loving partner and being so supportive to me. Thank you for being there for me and I am excited to see where life takes us in the future.

Aruna Indeewara Munasinghe

University of Kansas,

October, 2018

Table of Contents

Abbreviations and Acronyms

Abs	absorption
BDE	bond dissociation enthalpy
BDFE	bond dissociation free energy
DFT	density functional theory
CV	cyclic voltammetry
EPR	electron paramagnetic resonance
ESI-MS	electrospray ionization mass spectrometry
HAT	hydrogen atom transfer
KIE	kinetic isotope effect
MeCN	acetonitrile
NMR	nuclear magnetic resonance
OEC	oxygen evolving center
PhIO	iodosobenzene
UV	ultraviolet
Vis	visible
XRD	X-ray diffraction

Table of Tables

Table of Figures

Chapter 1. Proton Coupled Electron Transfer Reactions in Nature with Emphasis on the Mn-lipoxygenase Enzyme

1.1 Introduction

Proton coupled electron transfer (PCET) reactions are commonly observed in catalytic redox processes in biology[1-5] and synthetic chemistry.[2, 6] These reactions range from the common bioenergetic processes that power cells in nature to fossil fuel combustion that power machines in the modern world. In nature, the oxygen evolving complex (OEC) of Photosystem II found in thylakoid membranes of chloroplasts in plants and algae utilizes PCET reactions extensively.[7] This enzyme catalyzes the photooxidation of water into dioxygen where it undergoes a cycle of steps known as the Kok cycle, which involves transfer of $4H^+$ and $4e^-$ (four oxidizing equivalents). Most of the electron and proton transfer steps in the Kok cycle (at least in three steps) occur by PCET reactions.[2, 7-8] Another example is the Mn- and Fe-lipoxygenase systems in nature that catalyze the oxidation of polyunsaturated fatty acids (substrate). In this biological process, a concerted PCET step is employed to abstract a hydrogen atom from a weak C–H bond of the substrate in an energetically feasible manner.[9-11] The use of PCET reactions in nature is further demonstrated in cytochrome c oxidase enzymes in bacteria.[12] This membrane-bound protein catalyzes the $4e^-$ reduction of dioxygen undertaking the role as the terminal member of the cell respiratory chain.[2, 13] In addition to that, one of the more recent discoveries of utilization of PCET reactions in nature are the class Ia ribonucleotide reductase enzymes. These enzymes catalyze the conversion of nucleotides to deoxynucleotides in all organisms providing building blocks for replication of DNA.[2, 5, 14] During catalysis these enzymes are able to achieve forward and reverse PCET activity over a chain of redox active amino acids spanning a total distance higher than 35 Å.[5, 14-15]

In current literature, the term PCET is used to describe a broad spectrum of reactions in which transfer of both electrons and protons occur from one species to another in a single kinetic step or in a sequential manner.[6, 16] In general, any natural or synthetic PCET processes can be

categorized into two main categories, concerted and sequential proton coupled electron transfer reactions. In practice, the distinction between the two processes is not always clear, especially in ultrafast PCET processes.[16] Among many sub-categories of PCET, a hydrogen atom transfer (HAT) process is defined when the electron and proton transfer occur from the same donor to a single acceptor in a single kinetic step.

1.2 Thermodynamic background of HAT reactions

Hydrogen atom transfer reactions in organic chemistry have been studied for over a century, while HAT in transition metal complexes have being gaining attention of scientists for over three decades and has grown into a strong research area. The use of HAT reactions in nature is ubiquitous and enzymes such as lipoxygenase,[11, 17-18] ribonucleotide reductases[5] and methane monooxygenases rely on HAT processes in their mechanisms.[19] In metalloenzyme kinetics, HAT is recognized as an important phenomenon in maintaining an effective rate while keeping selectivity in catalytic reactions.[6] Thermodynamically, HAT reactions can be described as more favorable processes than their equivalent separated PCET processes as they avoid high energetic charged intermediates that are usually generated in separated PCET reactions.[20] Reaction **1** depicts a HAT reaction between HX and Y reactants.

$$HX + Y \longrightarrow X + HY \qquad 1.1$$

The thermochemistry of HAT reactions is governed by the acidity or basicity (K_a *or* K_b) of the oxidized (HY^+/Y) and reduced (HY/Y^-) forms, and the reduction potentials (E_{red}) of the deprotonated ($X^{\cdot}/X^-$) and protonated ($XH^{\cdot+}/XH$) substrate. In other words, a HAT reaction can be broken down to a separate electron and a proton transfer process as we describe a separated PCET reactions (Figure 1.1). The free energies of these individual steps can be mathematically expressed as follows (Equations 1.2 and 1.3),

$$\Delta G^{\circ}_{PT} = -RT ln(K_a) \quad 1.2$$

$$\Delta G^{\circ}_{ET} = -FE^{\circ} \quad 2.3$$

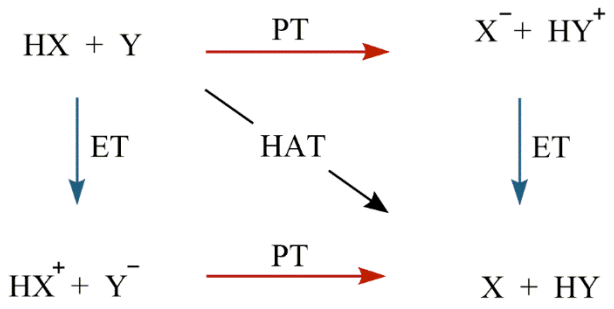

Figure 1.1 Thermodynamic scheme for possible pathways for PCET.

In a thermodynamic point of view, HAT reactivity can be mainly viewed to be dependent on the difference of the BDFEs between the formed and the broken bonds in the reaction. However it should be noted that factors like steric hindrances, the type of X atom and entropic changes associated with the hydrogen atom abstractor or the donor can alter HAT reactivity as well.[20] The correlation between the driving force of the reaction (using BDEs, ΔH°) and Eyring barrier of the HAT reaction (log k($M^{-1}s^{-1}$)) within a set of HAT reactions was first suggested by Evans and Polanyi for organic reaction interpretations.[21] However, it was also found to be useful in certain sets of HAT reactions involving transition metal complexes. For example the set of HAT reactions that cleaves the C–H bond of selected substrates by $[Ru(O)(bpy)_2py]^{2+}$.[22] However, with most transition metal complexes, in HAT reactivity, the $|\Delta S^{\circ}| \neq 0$[20, 23] and thus $\Delta H^{\circ} \neq \Delta G^{\circ}$ unlike in organic reactions, where $|\Delta S^{\circ}| \approx 0$[20, 24] and $\Delta H^{\circ} \approx \Delta G^{\circ}$. Due to this reason, it is preferred to use BDFE values to calculate the driving force for the HAT reactions.

As mentioned earlier, in a thermodynamic view point, a HAT reaction can be described by using a separate proton and an electron transfer process. Using this concept, in 1988, Bordwell developed an equation to determine BDEs of organic substrates.[25] Later on, this approach was extended by Tilset[26], Parker, and Wayner[27] where they included solvent contributions as well to calculate BDFEs. The modified Bordwell equation is as follows,

$$\boldsymbol{BDFE_{solv}(X-H) = 1.37pK_a + 23.06E^0 + C_{G,sol}} \qquad 3.4$$

1.3 Nature's utilization of HAT mechanisms, importance and reactivity of lipoxygenase

As mentioned earlier, various enzymatic systems utilize HAT mechanisms in carrying out redox reactions. Among them, lipoxygenase is a mononuclear oxygen dependent non-heme metalloenzyme that can be found in a variety of plants, animals and fungi. Except for few exceptions, lipoxygenase enzymes can catalyze the oxidation of polyunsaturated fatty acids with one or more cis,cis-1,4-pentadiene units into hydroperoxides.[10] These enzymes have a variety of biomedical applications, such as production of leukotrienes and lipoxins to regulate inflammatory conditions and cancer.[28-29]

Lipoxygenases use Fe and Mn metals as the active site metal in carrying out catalytic reactions. Kinetic isotope effects (k_H/k_D) as large as ~50[30] (for Fe-LOXs) and 21-24[31] (for Mn-LOXs) are observed for these enzymes and these values indicate a strong tunneling nature occurring in HAT reactivity of these enzymes.

The Mn-LOX is particularly a unique example in nature for use of mid valent Mn^{III} centers in carrying out C–H bond oxidation. The active site of Mn-LOX (Figure 1.2) consists of two histidine residues, an asparagine residue and a valine residue at the equatorial positions in the active site. The val residue is bound from the carboxylate oxygen of the C-terminus of the molecule. One of the axial positions is occupied by a histidine residue while the second active site remains as the vacant site of the active site where the catalytic reaction occurs.[32] The proposed catalytic cycle of Mn-LOX system is depicted in Figure 1.3.

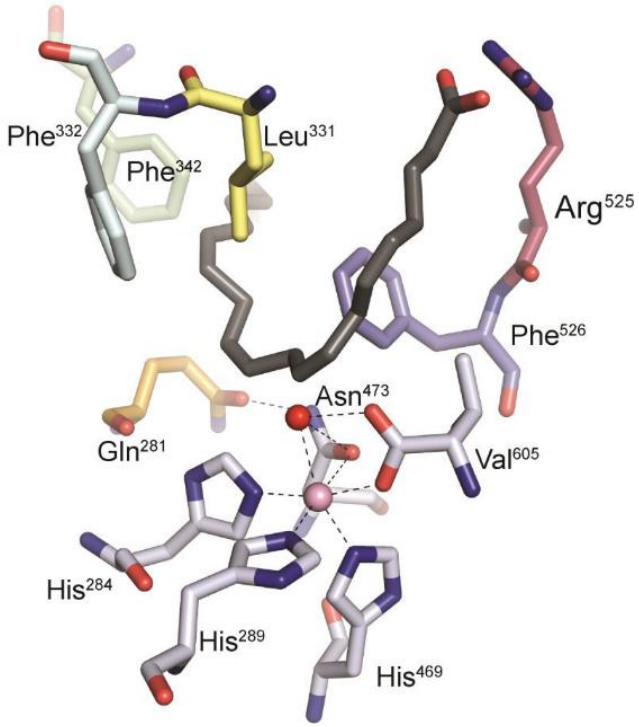

Figure 1.2 Substrate bound active site of Mo-MnLOX of fungus Magnaporthe oryzae (Mo).[32]

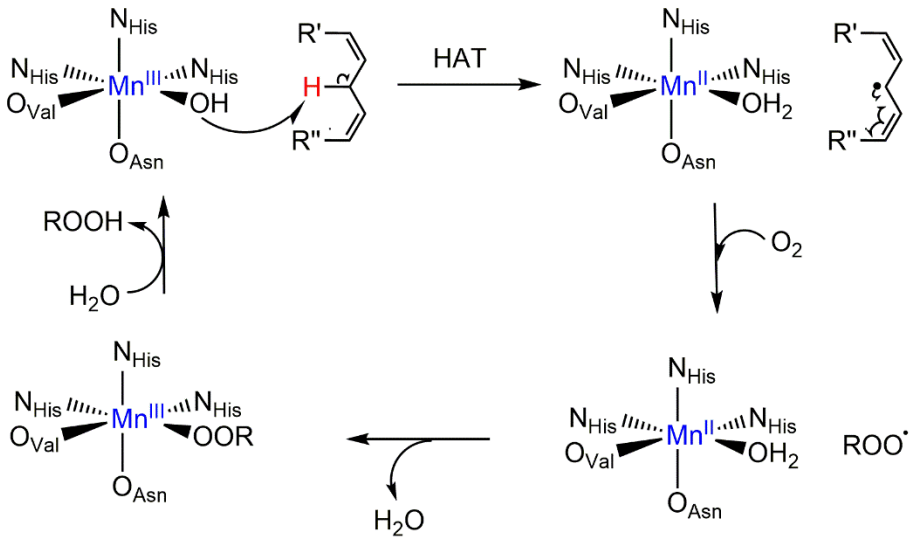

Figure 1.3 Schematic diagram of the catalytic cycle of Mn-LOX enzyme when it reacts with cis,cis-1,4-pentadiene containing fatty acids to produce alkyl hydroperoxides.[9]

The proposed mechanism of Mn-LOX reactivity has been influenced by the analogous mechanism of Fe-LOX that has been more extensively studied over the years.[9, 11, 33] Initially an H atom is abstracted from the C–H bond of the substrate by the Mn^{III}–OH unit in a single kinetic step. In this step, a proton is transferred to the oxygen atom in the –OH unit while an electron is transferred to the Mn^{III} center. As mentioned previously, a large substrate H/D kinetic isotope effect (k_H/k_D) of 21-24 was observed for the reaction of Mn-lipoxygenase with [U-^{2}H]linoleic acid obtained from stopped flow kinetic data.[31] It should also be noted that this hydrogen atom transfer step has been shown to be the rate-limiting step above 32 ˚C in the case of soybean lipoxygenase-1 (Fe-LOX).[30] As a result of this HAT step, a Mn^{II}–OH_2 moiety and a radical intermediate of the substrate is formed at the active site. This step is partly supported by the observed radical character in the EPR signal on a quenched sample of the reaction between Mn^{II}–LOX with linoleic acid at low temperature.[31] Consequently, an oxygen molecule is taken up by the radical substrate to form an alkylperoxy radical species. Alternatively, it has also been suggested that an initial activation

of molecular oxygen by the active site could occur followed by attack of an activated oxygen species upon the radical substrate.[34] However no solid evidence has been observed yet to support the formation of a activated oxygen species. Consequently, the radical species formed replaces the H_2O ligand on the Mn^{II} center to form a Mn^{III}–OOR intermediate species. Finally, a proton is abstracted from a water molecule to form the final product, a hydroperoxide species of the substrate. In the same step, the remaining hydroxyl group of the water molecule combines with the Mn^{III} center to form a Mn^{III}–OH moiety regenerating the starting material.

1.4 References

1. Kaila, V. R. I.; Verkhovsky, M. I.; Wikström, M., Proton-Coupled Electron Transfer in Cytochrome Oxidase. *Chemical Reviews* **2010,** *110* (12), 7062-7081.

2. Weinberg, D. R.; Gagliardi, C. J.; Hull, J. F.; Murphy, C. F.; Kent, C. A.; Westlake, B. C.; Paul, A.; Ess, D. H.; McCafferty, D. G.; Meyer, T. J., Proton-coupled electron transfer. *Chem Rev* **2012,** *112* (7), 4016-93.

3. Dempsey, J. L.; Winkler, J. R.; Gray, H. B., Proton-Coupled Electron Flow in Protein Redox Machines. *Chemical Reviews* **2010,** *110* (12), 7024-7039.

4. Sjödin, M.; Styring, S.; Wolpher, H.; Xu, Y.; Sun, L.; Hammarström, L., Switching the Redox Mechanism: Models for Proton-Coupled Electron Transfer from Tyrosine and Tryptophan. *Journal of the American Chemical Society* **2005,** *127* (11), 3855-3863.

5. Stubbe, J.; Nocera, D. G.; Yee, C. S.; Chang, M. C. Y., Radical Initiation in the Class I Ribonucleotide Reductase: Long-Range Proton-Coupled Electron Transfer? *Chemical Reviews* **2003,** *103* (6), 2167-2202.

6. Warren, J. J.; Tronic, T. A.; Mayer, J. M., Thermochemistry of Proton-Coupled Electron Transfer Reagents and its Implications. *Chemical Reviews* **2010,** *110* (12), 6961-7001.

7. Meyer, T. J.; Huynh, M. H. V.; Thorp, H. H., The Possible Role of Proton-Coupled Electron Transfer (PCET) in Water Oxidation by Photosystem II. *Angewandte Chemie International Edition* **2007,** *46* (28), 5284-5304.

8. Hoganson, C. W.; Babcock, G. T., A Metalloradical Mechanism for the Generation of Oxygen from Water in Photosynthesis. *Science* **1997,** *277* (5334), 1953-1956.

9. Wennman, A.; Karkehabadi, S.; Oliw, E. H., Kinetic investigation of the rate-limiting step of manganese- and iron-lipoxygenases. *Arch. Biochem. Biophys.* **2014,** *555-556*, 9-15.

10. Wennman, A.; Magnuson, A.; Hamberg, M.; Oliw, E. H., Manganese lipoxygenase of F. oxysporum and the structural basis for biosynthesis of distinct 11-hydroperoxy stereoisomers. *Journal of Lipid Research* **2015,** *56* (8), 1606-1615.

11. Hatcher, E.; Soudackov, A. V.; Hammes-Schiffer, S., Proton-Coupled Electron Transfer in Soybean Lipoxygenase. *Journal of the American Chemical Society* **2004,** *126* (18), 5763-5775.

12. Babcock, G. T., How oxygen is activated and reduced in respiration. *Proc Natl Acad Sci U S A* **1999,** *96* (23), 12971-3.

13. Verkhovsky, M. I.; Belevich, I.; Bloch, D. A.; Wikström, M., Elementary steps of proton translocation in the catalytic cycle of cytochrome oxidase. *Biochimica et Biophysica Acta (BBA) - Bioenergetics* **2006,** *1757* (5-6), 401-407.

14. Stubbe, J.; van der Donk, W. A., Protein Radicals in Enzyme Catalysis. *Chemical Reviews* **1998,** *98* (2), 705-762.

15. Uhlin, U.; Eklund, H., Structure of ribonucleotide reductase protein R1. *Nature* **1994,** *370* (6490), 533-539.

16. Hammes-Schiffer, S., Introduction: Proton-Coupled Electron Transfer. *Chemical Reviews* **2010,** *110* (12), 6937-6938.

17. Liang, Z.-X.; Klinman, J. P., Structural bases of hydrogen tunneling in enzymes: progress and puzzles. *Current Opinion in Structural Biology* **2004,** *14* (6), 648-655.

18. Goldsmith, C. R.; Stack, T. D. P., Hydrogen Atom Abstraction by a Mononuclear Ferric Hydroxide Complex: Insights into the Reactivity of Lipoxygenase. *Inorganic Chemistry* **2006,** *45* (15), 6048-6055.

19. Ragsdale, S. W., Metals and Their Scaffolds To Promote Difficult Enzymatic Reactions. *Chemical Reviews* **2006,** *106* (8), 3317-3337.

20. Mayer, J. M., Understanding Hydrogen Atom Transfer: From Bond Strengths to Marcus Theory. *Accounts of Chemical Research* **2011,** *44* (1), 36-46.

21. Evans, M. G.; Polanyi, M., Inertia and driving force of chemical reactions. *Transactions of the Faraday Society* **1938,** *34*.

22. Matsuo, T.; Mayer, J. M., Oxidations of NADH Analogues bycis-[RuIV(bpy)2(py)(O)]2+Occur by Hydrogen-Atom Transfer Rather than by Hydride Transfer. *Inorganic Chemistry* **2005,** *44* (7), 2150-2158.

23. Mader, E. A.; Davidson, E. R.; Mayer, J. M., Large Ground-State Entropy Changes for Hydrogen Atom Transfer Reactions of Iron Complexes. *Journal of the American Chemical Society* **2007,** *129* (16), 5153-5166.

24. Warren, J. J.; Mayer, J. M., Predicting organic hydrogen atom transfer rate constants using the Marcus cross relation. *Proceedings of the National Academy of Sciences* **2010,** *107* (12), 5282-5287.

25. Bordwell, F. G.; Cheng, J. P.; Harrelson, J. A., Homolytic bond dissociation energies in solution from equilibrium acidity and electrochemical data. *Journal of the American Chemical Society* **1988,** *110* (4), 1229-1231.

26. Tilset, M., *Electron Transfer in Chemistry*. Weinheim: Wiley-VCH: 2001; p 677-713.

27. Wayner, D. D. M.; Parker, V. D., Bond energies in solution from electrode potentials and thermochemical cycles. A simplified and general approach. *Accounts of Chemical Research* **1993,** *26* (5), 287-294.

28. Samuelsson, B.; Dahlen, S.; Lindgren, J.; Rouzer, C.; Serhan, C., Leukotrienes and lipoxins: structures, biosynthesis, and biological effects. *Science* **1987,** *237* (4819), 1171-1176.

29. Nelson, M. J.; Seitz, S., In *Active Oxygen in Biochemistry*, Valentine, J. S.; Foote, C. S.; Greenberg, A.; Liebman, J. F., Eds. Chapman and Hall: Glasgow, U.K., 1995; pp 276-312.

30. Glickman, M. H.; Klinman, J. P., Nature of Rate-Limiting Steps in the Soybean Lipoxygenase-1 Reaction. *Biochemistry* **1995,** *34* (43), 14077-14092.

31. Su, C.; Sahlin, M.; Oliw, E. H., Kinetics of Manganese Lipoxygenase with a Catalytic Mononuclear Redox Center. *Journal of Biological Chemistry* **2000,** *275* (25), 18830-18835.

32. Wennman, A.; Oliw, E. H.; Karkehabadi, S.; Chen, Y., Crystal Structure of Manganese Lipoxygenase of the Rice Blast Fungus Magnaporthe oryzae. *Journal of Biological Chemistry* **2016,** *291* (15), 8130-8139.

33. Rickert, K. W.; Klinman, J. P., Nature of Hydrogen Transfer in Soybean Lipoxygenase 1: Separation of Primary and Secondary Isotope Effects†. *Biochemistry* **1999,** *38* (38), 12218-12228.

34. Petersson, L.; Slappendel, S.; Vliegenthart, J. F. G., The magnetic susceptibility of native soybean lipoxygenase-1. Implications for the symmetry of the iron environmental and the possible coordination of dioxygen to Fe(II). *Biochimica et Biophysica Acta (BBA) - Protein Structure and Molecular Enzymology* **1985,** *828* (1), 81-85.

Chapter 2: Preparation, structural characterization and HAT reactivity of the Mn-dpaq^{5Cl} system

This work has been reproduced in part from: Rice, D. B; Munasinghe, A. I; Grotemeyer, E.; Burr, A.; Day, V.; Jackson, T.A., Structure and Reactivity of (μ-oxo)dimanganese(III,III) and Mononuclear Hydroxomanganese(III) Adducts Supported by Derivatives of an Amide-containing Pentadentate Ligand. *Inorganic Chemistry*, Manuscript ID: ic-2018-027944

2.1 Introduction

Proton coupled electron transfer (PCET) reactions are ubiquitous in biological systems. Among different types of PCET reactions, a process where the transfer of a proton and an electron occurs in the same kinetic step is called a hydrogen atom transfer (HAT) reaction.[1] In many of these reactions, high-valent metal-oxo moieties have been observed to be the most common H-atom abstraction agent. However, in recent years there has been an increase of attention in both high- and mid-valent metal-hydroxo species that can oxidize weak C–H and O–H bonds at comparably low reduction potentials ($E_{1/2}$).[2] For example, the Fe and Mn lipoxygenase (LOX) enzymes contain Fe^{III}–OH and Mn^{III}–OH units that can attack a C–H bond of a cis, cis-1,4-pentadiene containing polyunsaturated fatty acid with a bond dissociation free energy ($BDFE_{C\text{-}H}$) of 77 kcal/mol. The substrate is converted into an alkyl hydro-peroxide in the process. During the catalytic cycle of Fe- and Mn-LOX, the metal-hydroxo species reacts with the substrate with a large substrate H/D kinetic isotope effect (>21[3]) suggesting a HAT pathway with a significant tunneling effect.

The chemistry of Fe- and Mn-LOX has inspired a number of Fe^{III}-hydroxo and Mn^{III}-hydroxo model systems. Using both heme and nonheme supporting ligands, a variety of groups have described the ability of mononuclear Fe^{III}-hydroxo complexes to perform HAT reactions with hydrocarbons. Some of these complexes are excellent oxidants. For example, the recently reported $[Fe^{III}(OH)(OH_2)(PyPz)]^{4+}$ (PyPz = tetramethyl-2,3-pyridino porphyrazine) complex displayed a second-order rate constant for DHA oxidation that far exceeds that of many high-valent Fe-oxo species.[4] In contrast, the number of Mn^{III}-hydroxo units known to attack C–H bonds of any strength is extremely limited. The $[Mn^{III}(OH)(PY5)]^{+}$ complex of Stack and Goldberg (Figure 1, top left) remains the most impressive synthetic Mn^{III}-hydroxo unit for HAT reactions.[5] This

complex is capable of oxidizing the relatively strong C–H bond of toluene (BDFE of 87 kcal/mol in CH_3CN[2]), albeit slowly. In contrast, the $[Mn^{III}(OH)(S^{Me2}N_4(tren))]^+$ complex of Kovacs and co-workers (Figure 2.1, top right) was limited in the scope of its reactivity, being only capable of attacking the activated O–H bond of TEMPOH (O–H BDFE in CH_3CN of 66.5 kcal/mol[2]) but doing so with a rapid rate.[6]

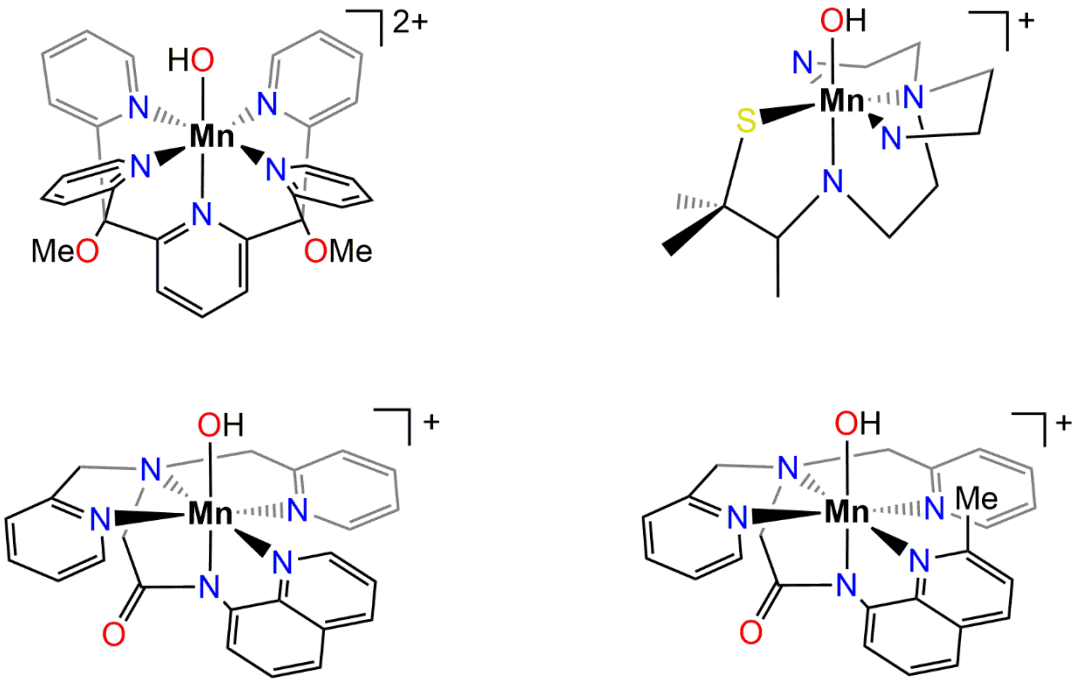

Figure 2.1 Comparison of molecular structures of $[Mn^{III}(OH)(PY5)]^{2+}$ (top left),[5] $[Mn^{III}(OH)(S^{Me2}N_4(tren))]^+$ (top right)[6], $[Mn^{III}(OH)(dpaq)]^+$ (bottom left)[7] and $[Mn^{III}(OH)(dpaq^{2Me})]^+$ (bottom right).[8]

Our lab has reported a pair of Mn^{III}-hydroxo complexes, supported by amide-containing pentadentate ligands (Figure 1, bottom), with HAT abilities intermediate between those of the $[Mn^{III}(OH)(PY5)]^+$ and $[Mn^{III}(OH)(S^{Me2}N_4(tren))]^+$ complexes.[7-8] Although the rates of TEMPOH oxidation by $[Mn^{III}(OH)(dpaq)]^+$ and $[Mn^{III}(OH)(dpaq^{2Me})]^+$ are ca. 100-fold slower than that of

$[Mn^{III}(OH)(S^{Me2}N_4(tren))]^+$, the former complexes are capable of attacking substrates with stronger O–H and C–H bonds. For example, both $[Mn^{III}(OH)(dpaq)]^+$ and $[Mn^{III}(OH)(dpaq^{2Me})]^+$ oxidize xanthene (C–H BDFE of 73.3 kcal/mol in DMSO[2]), with rates only ca. 10 to 30-fold slower than that of $[Mn^{III}(OH)(PY5)]^+$.[7-8] Among the $[Mn^{III}(OH)(dpaq)]^+$ and $[Mn^{III}(OH)(dpaq^{2Me})]^+$ complexes, the latter was originally reported to be a more reactive HAT agent towards sterically unencumbered substrates.[8] However, the initial kinetic investigations of $[Mn^{III}(OH)(dpaq)]^+$ were complicated by an equilibrium between this complex and a spin-coupled antiferromagnetically coupled species.[9] Analysis of the ^{1}H-NMR signals of this species, along with low-temperature Mn K-edge X-ray absorption experiments, suggest that the antiferromagnetically coupled species is the dimeric $[Mn^{III}Mn^{III}(\mu\text{-}O)(dpaq)_2]^{2+}$ complex.

It is important and interesting to look at a variety of geometries and electronic structures and their impact on HAT reactions. However current systems have many factors changing between complexes. For example the comparatively more sterically encumbered Stack's complex have an overall 2+ charge while others are only have 1+ charges. On the other hand, the Kovacs complex with a sulfur atom occupying one of the equatorial positions is the least sterically encumbered complex of the set. The $[Mn^{III}(OH)(dpaq^{R})](OTf)$, (R=H, 2Me) complexes are monocationic complexes with moderate steric hindrances. Under such conditions it may prove to be difficult to gain a general understanding of the factors that govern HAT reactions. Therefore more synthetic models with systematic changes to the geometry and electronic structure are needed to better understand the natural systems. The objective of this study is to extend the previously reported dpaq system with a perturbation to its electronic structure and examining how HAT reactivity and thermodynamic parameters of the complex are altered. Herein, investigated the preparation and characterization of a new addition to the Mn–dpaq series, $[Mn^{III}(OH)dpaq^{5Cl}](OTf)$. The

$[Mn^{III}(OH)(dpaq^{R})](OTf)$ series consists species with minor alterations in geometry and electronic structure that can undergo well behaved HAT reaction. This provides the perfect opportunity to study the relationships between geometry, structure and their effects on the thermodynamics in HAT.

2.2 Materials and Method

2.2.1 Materials and Instrumentation. All solvents and chemicals were obtained from commercial vendors at ACS grade or better and, unless described otherwise, were used without further purification. Acetonitrile and ether were dried and degassed using a Pure Solv (2010) solvent purification system, as described previously. The $Hdpaq^{5Cl}$ ligand, $[Mn^{II}(CH_3CN)_2(OTf)_2]_n$ salt, and TEMPOH were generated by previously reported methods.[7-8, 10-12] All ^1H NMR spectra were collected on a 400 MHz Bruker AVIIIHD NMR with an acquisition time of 0.27 s and a spectral width of 150 ppm to – 7 ppm. At least 1000 scan were collected to provide sufficient S/N. Spectra were baseline-subtracted with the multipoint fitting procedure using spline functions as available in MestReNova. Mass spectrometry and EPR experiments were collected on previously described instrumentation.[9]

2.2.2 Preparation and Characterization of $[Mn^{II}(dpaq^{5Cl})(OTf)]$. All syntheses and manipulations of Mn^{II} complexes were performed in an Ar-filled glovebox. The $[Mn^{II}(dpaq^{5Cl})(OTf)]$ complex was prepared by analogy to methods reported for the perchlorate salt,[13] with the change that metalation reaction was performed using $[Mn^{II}(CH_3CN)_2(OTf)_2]_n$. The $[Mn^{II}(dpaq^{5Cl})(OTf)]$ complex was purified by recrystallization in CH_3CN:Et_2O and then oxidized to form their Mn^{III} analogues by the procedures described below. The composition of $[Mn^{II}(dpaq^{5Cl})(OTf)]$ was further determined by ESI-MS: m/z = 471.0514 (calculated m/z = 471.0514 for $([Mn^{II}(dpaq^{5Cl})]^+$). μ_{eff} (Evan's NMR) = 5.90 μ_B (calculated μ_{eff} =5.92 μ_B for a high-

spin S = 5/2 Mn^{II} center). The EPR spectrum of a 1.25 mM [Mn^{II}($dpaq^{5Cl}$)(OTf)] in CH_3CN measured at 10 K showed a broad isotropic signal with a g value of 2.00 (Figure 2.4).

2.2.3 Preparation and Characterization of (μ-oxo)dimanganese(III,III) and hydroxomanganese(III) Complexes. A solution of 55 mg (88 μmol) crystalline [Mn^{II}($dpaq^{5Cl}$)(OTf)] was prepared in 2 mL dried CH_3CN in a glove box. Solid iodosobenzene (9.7 mg; 44 μmol) was added to this solution, and the reaction mixture was stirred for 12 hours. The resulting solution was evaporated to dryness under vacuum. This solid was dissolved in a minimum amount of CH_3CN and subjected to repeated recrystallizations by vapor diffusion with Et_2O. The procedure yielded needle like, dark-brown crystals of [$Mn^{III}Mn^{III}$(μ-O)($dpaq^{5Cl}$)$_2$](OTf)$_2$ (30 mg; 55% yield), suitable for X-ray diffraction analysis. The solid-phase composition of this complex was also supported by elemental analysis: found (%): C 45.51, H 3.36, N 11.00; calcd.(%): C 45.84, H 3.05, N 11.14. The solution-phase composition of [$Mn^{III}Mn^{III}$(μ-O)($dpaq^{5Cl}$)$_2$](OTf)$_2$ was analyzed by ^{1}H NMR spectroscopy and the Evan's NMR method, both in acetonitrile. The ^{1}H NMR spectrum of [$Mn^{III}Mn^{III}$(μ-O)($dpaq^{5Cl}$)$_2$](OTf)$_2$ dissolved in dried CD_3CN (with a concentration of 37(10) ppm or (2.1(5) mM of H_2O) showed chemical shifts (Figure 2.7) in the diamagnetic range (0 to 30 ppm), which we attribute to [$Mn^{III}Mn^{III}$(μ-O)($dpaq^{5Cl}$)$_2$](OTf)$_2$. A set of nine weak signals observed outside this chemical shift range are attributed to [Mn^{III}(OH)($dpaq^{5Cl}$)]$^+$, which is generated from the reaction of [$Mn^{III}Mn^{III}$(μ-O)($dpaq^{5Cl}$)$_2$](OTf)$_2$ with water. In support, the effective magnetic moment of a CD_3CN (with a concentration of 37(10) ppm or (2.1(5) mM of H_2O) solution [$Mn^{III}Mn^{III}$(μ-O)($dpaq^{5Cl}$)](OTf)$_2$ was determined to be 1.88 μ_B per Mn. The solid state magnetic moment of this complex by the Gouy method using a magnetic susceptibility balance yielded 1.18 μ_B per Mn.

2.2.4 Preparation of [Mn^{III}(OH)($dpaq^{5Cl}$)](OTf). A 2.5 mM [Mn^{II}($dpaq^{5Cl}$)(OTf)] solution was prepared in 2 mL of CH_3CN in a glove box. This solution was transferred to a cuvette that was sealed with a rubber septum and then removed from the glove box. This solution was stirred and monitored by electronic absorption spectroscopy, during which O_2(g) was bubbled through the solution. A dark-brown solution was formed, with optical changes completed in 5 hours. On the basis of ^{1}H NMR and electronic absorption data (*vide infra*), this solution contains a mixture of [$Mn^{III}Mn^{III}$(μ-O)($dpaq^{5Cl}$)$_2$]$^{2+}$ and [Mn^{III}(OH)($dpaq^{5Cl}$)]$^+$. To isolate the [Mn^{III}(OH)($dpaq^{5Cl}$)]$^+$ species, 560 equivalents of water were added to the solution of [$Mn^{III}Mn^{III}$(μ-O)($dpaq^{5Cl}$)$_2$]$^{2+}$ and [Mn^{III}(OH)($dpaq^{5Cl}$)]$^+$, and the color of the solution changed from dark-brown to orange. Electronic absorption and ^{1}H NMR data (*vide infra*) show that the [Mn^{III}(OH)($dpaq^{5Cl}$)]$^+$ species is the dominant species in solution under these conditions. To obtain quantities of [Mn^{III}(OH)($dpaq^{5Cl}$)](OTf) suitable for bulk characterization, the above synthesis was carried out on a larger scale. A stirred solution of 50 mg (78 μmol) of crystalline [Mn^{II}($dpaq^{5Cl}$)(OTf)] in 2 mL of CH_3CN was prepared and stirred overnight under an O_2(g) atmosphere. The resulting solution was evaporated to dryness and then dissolved in a minimum amount of 90:10 CH_3CN:H_2O (vol:vol). Brown-orange crystalline plates of [Mn^{III}(OH)dpaq^{5Cl}](OTf), suitable for X-ray diffraction analysis, were obtained with good yield (90%) after three re-crystallizations by vapor diffusion of Et_2O into the concentrated 90:10 CH_3CN:H_2O (vol:vol) solution. The composition of [Mn^{III}(OH)($dpaq^{5Cl}$)](OTf) was further determined by a variety of methods. μ_{eff} (by Evan's NMR) = 4.91 μ_B (calculated μ_{eff} = 4.90 μ_B for a high-spin S = 2 Mn^{III} center). ESI-MS: m/z = 488.0683 (calculated m/z = 488.24 for ([Mn^{III}(OH)($dpaq^{5Cl}$)]$^+$); Elemental analysis [Mn^{III}(OH)($dpaq^{5Cl}$)](OTf)(MeCN)(H_2O): found (%): C 44.72, H 3.50, N 12.23; calcd.(%): C 44.81, H 3.62, N 12.06.

2.2.5 Kinetic Studies of TEMPOH oxidation by [Mn^{III}(OH)($dpaq^{5Cl}$)](OTf). All kinetic experiments were performed using an Agilent 8453 spectrometer. In a glovebox, a 1.25 mM [Mn^{III}(OH)($dpaq^{5Cl}$)]$^+$ solution was prepared in 2 mL of acetonitrile and transferred to a cuvette that was sealed with a rubber septum. The cuvette was removed from the glovebox, at which point a 100 μL aliquot of a 60:40 CH_3CN:H_2O (vol:vol) solution, purged with nitrogen, were added using a gastight syringe that had been purged with Ar(g) before use. This addition delivers 880 equivalents of water per Mn, ensuring that the Mn^{III}-hydroxo species is dominant in solution. This solution was equilibrated at -35 ˚C for at least 10 minutes using a Unisoku cryostat. Stock solutions of TEMPOH were prepared in 500 μL of CH_3CN in a glove box. The concentrations of these solutions were such that the addition of a 100 μL aliquot to the 2 mL solution of 1.25 mM [Mn^{III}(OH)($dpaq^{5R}$)]$^+$ delivers 10 – 40 equivalents of TEMPOH per Mn. The 100 μL aliquots of TEMPOH solution were contained in gastight syringes with the needles sealed by a rubber septum. These syringes were removed from the glovebox, at which point they were immediately added to the solution of [Mn^{III}(OH)($dpaq^{5Cl}$)]$^+$ maintained at -35 ˚C. The addition of TEMPOH led to the rapid disappearance of the electronic absorption signatures of [Mn^{III}(OH)($dpaq^{5Cl}$)]$^+$. A pseudo-first-order decay rate (k_{obs}) for this process was determined by fitting the change in absorbance at approximately 770 nm as a function of time. The final reaction mixture was analyzed by perpendicular-mode X-band EPR spectroscopy at 10 K; the EPR spectrum showed a characteristic signal consistent with a TEMPO radical.

2.2.6 Cyclic Voltammetry for [Mn^{III}(OH)($dpaq^{5Cl}$)](OTf). Cyclic voltammetry (CV) data was collected for a 1.0 mM solution of [Mn^{III}(OH)($dpaq^{5Cl}$)](OTf) derivative in 98:2 (vol:vol) CH_3CN:H_2O. All CV experiments were performed under an inert atmosphere. Solvents were purged with nitrogen to remove oxygen until no redox peaks related to oxygen were observed. A

Ag/AgCl quasi-reference electrode, a platinum auxiliary electrode, and a glassy carbon electrode were used as the three electrode system, with 0.1 M $Bu_4N(PF_6)$ as the supporting electrolyte. Peak position was referenced to the Fc^+/Fc couple, which was collected under identical experimental conditions. Conversion of the Fc^+/Fc potential in CH_3CN to SCE employed a correction of +0.38 V.[14]

2.3 Results and Discussion

Structure and Properties of [$Mn^{II}(dpaq^{5Cl})(OTf)$] complex. The X-ray crystal structure of [$Mn^{II}(dpaq^{5Cl})(OTf)$] shows the Mn^{II} ion in a distorted octahedral environment, with the nitrogen atoms from the quinolinyl, pyridyl, and amine groups forming the equatorial plane, and the amide nitrogen and triflate oxygen in the axial positions (Figure 2.2). The Mn-ligand bond lengths and selected coordination angles collected from XRD data are summarized in Table 2.1, which also includes corresponding parameters for the previously reported [$Mn^{II}(dpaq)](OTf)$[7] and [$Mn^{II}(dpaq^{2Me})](OTf)$.[8] The most conspicuous difference in the XRD structure of [$Mn^{II}(dpaq^{5Cl})(OTf)$] compared to these other complexes is that the former two complexes showed polymeric structures, where the axial position *trans* to the amide nitrogen of one $[Mn^{II}(dpaq)]^+$ moiety was occupied by a carbonyl oxygen from a separate $[Mn^{II}(dpaq)]^+$ or $[Mn^{II}(dpaq^{2Me})]^+$ unit. This difference presumably arises from the presence of steric bulk generated by the 5-chloro-quinolinyl group of the $dpaq^{5Cl}$ ligand.

In addition to the above major difference, the structure of [$Mn^{II}(dpaq^{5Cl})(OTf)$] has noticeable distinctions from $[Mn^{II}(dpaq)]^+$ and $[Mn^{II}(dpaq^{2Me})]^+$. For example, the distance Mn–N2 is shorter by ~0.04 Å than that of in $[Mn^{II}(dpaq)]^+$. In addition to that, the N2–Mn^{II}–O11 bond angle is narrower by about 5˚ when compared to $[Mn^{II}(dpaq)]^+$. This reduced linearity of the N2–Mn^{II}–O11

bond in [Mn^{II}($dpaq^{5Cl}$)(OTf)] can be attributed to the decreased steric bulk that's imposed on the ligand system when compared to the polymeric [Mn^{II}(dpaq)]$^{+}$ structure.

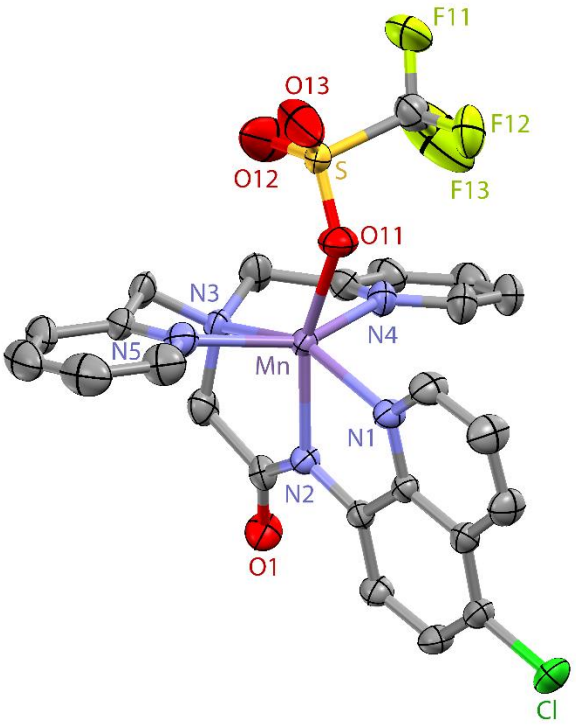

Figure 2.2 ORTEP diagram of [Mn^{II}($dpaq^{5Cl}$)(OTf)]. Protons have been removed for clarity.

Table 2.1 Selected Manganese-Ligand Bond Lengths (Å) and Coordination Angles from the Crystal Structures of [Mn^{II}($dpaq^{5Cl}$)(OTf)], [Mn^{II}(dpaq)](OTf),[7] and [Mn^{II}($dpaq^{2Me}$)](OTf).[8]

[Mn^{II}($dpaq^{R}$)](OTf)			
	R = 5Cl	R = H	R = 2Me
Mn–O1	2.196(2)	2.079(2)	2.116(2)
Mn–N1	2.248(2)	2.214(3)	2.268(3)
Mn–N2	2.146(2)	2.191(3)	2.172(3)
Mn–N3	2.329(2)	2.314(3)	2.317(3)
Mn–N4	2.239(3)	2.244(3)	2.275(3)

Mn–N5	2.253(3)	2.286(3)	2.286(3)
N2–Mn^{II}–O1	159.43(9)°	164.88(10)°	170.35°
N4–Mn^{II}–N5	144.80(9)°	147.89(11)°	149.03°
N1–Mn^{II}–N3	153.16(8)°	151.40(10)°	150.56°
N4–Mn^{II}–N2	89.22(8)°	94.97(10)°	87.33°
N1–Mn^{II}–N2	74.71(9)°	74.46(10)°	74.59°
N3–Mn^{II}–N2	78.47(9)°	77.52(10)°	76.41°

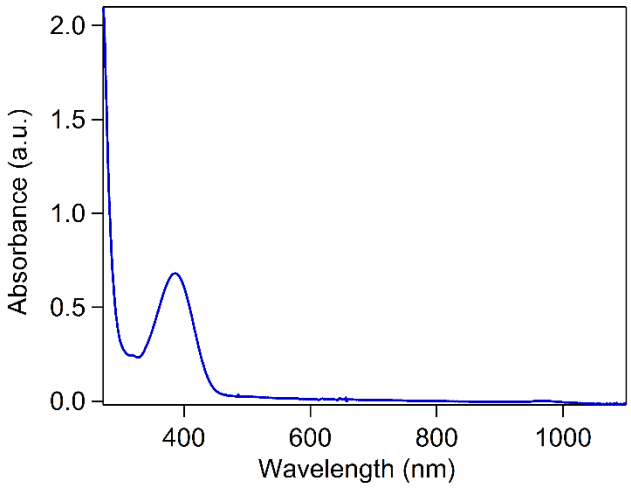

Figure 2.3 UV-Vis spectrum of a solution of 0.125 mM $[Mn^{II}(dpaq^{5Cl})]^{+}$ prepared in CH_3CN.

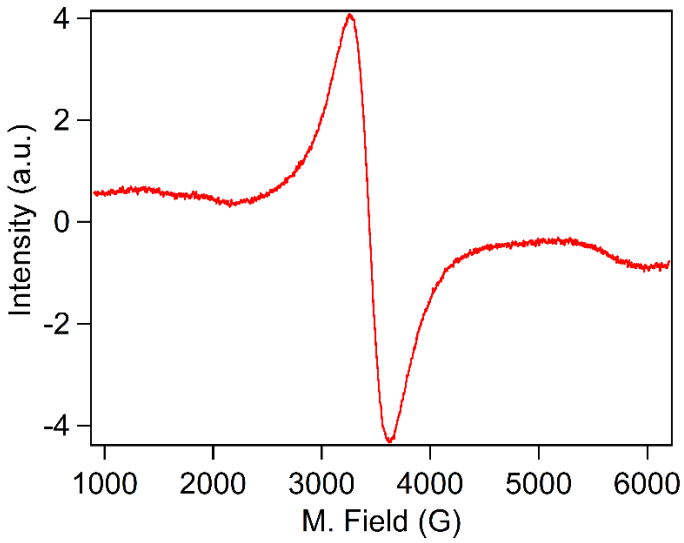

Figure 2.4 Perpendicular-mode X band EPR spectrum of a solution of 1.25 mM [Mn^{II}($dpaq^{5Cl}$)(OTf)] prepared in CH_3CN measured at 10 K.

The electronic absorption spectrum of [Mn^{II}($dpaq^{5Cl}$)(OTf)] in CH_3CN (Figure 2.3) shows an intense band at 388 nm (ε = 5 400 $M^{-1}cm^{-1}$) and a weak band at 520 nm (ε = 32 $M^{-1}cm^{-1}$). The electronic absorption spectrum of the previously reported [Mn^{II}($dpaq^{5Cl}$)(ClO_4)] complex in CH_3CN likewise showed an intense band at 388 nm with an extinction coefficient close to that reported here (5 330 $M^{-1}cm^{-1}$).[13] The essentially identical optical properties of these complexes strongly suggests that the axial triflate and perchlorate ligands of [Mn^{II}($dpaq^{5Cl}$)(OTf)] and [Mn^{II}($dpaq^{5Cl}$(ClO_4)], respectively, are replaced by CH_3CN upon dissolution. A perpendicular-mode X-band EPR spectrum of a frozen solution of [Mn^{II}($dpaq^{5Cl}$)(OTf)] in CH_3CN at 10 K shows a broad isotropic feature centered at g = 2.00 that lacks any hyperfine splitting. Similarly broad and uninformative signals near g = 2.00 were observed for [Mn^{II}(dpaq)](OTf) and [Mn^{II}($dpaq^{2Me}$)](OTf) complexes.[7-8]

Oxidation of [Mn^{II}($dpaq^{5Cl}$)(OTf)]. Oxygenation of the [Mn^{II}($dpaq^{5Cl}$)(OTf)] complex in CH_3CN leads to the appearance of new electronic absorption features in the visible region (Figure

2.5). The electronic absorption of this solution show features at 550 nm and 770 nm. The addition of 560 equiv. of water to the oxygenated solution of [Mn^{II}($dpaq^{5Cl}$)(OTf)] causes the electronic absorption bands to sharpen, and the maxima of the higher-energy band blue-shifts to 500 nm (from 550 nm) (Figure 2.5). The nature of the oxygenation products, and the influence of water, can be understood on the basis of ^{1}H NMR experiments (Figure 2.5-2.7) and by analogy to a recent investigation of the oxygenation products of [Mn^{II}(dpaq)](OTf).[9] The electronic absorption features initially observed upon reaction of [Mn^{II}($dpaq^{5Cl}$)(OTf)] with O_2 are similar in energy and intensity to those observed when [Mn^{II}(dpaq)](OTf) is reacted with O_2 in CH_3CN (λ_{max} = 550 and 780 nm).[7] In that case, the electronic absorption spectrum was revealed to contain contributions from both the mononuclear [Mn^{III}(OH)(dpaq)]$^+$ species, as well as an antiferromagnetically coupled species, which we formulated as [$Mn^{III}Mn^{III}$(μ-O)$(dpaq)_2$]$^{2+}$.[9] The addition of water caused a shift in the equilibrium between these components to favor the Mn^{III}-hydroxo complex. Likewise, it can be presumed that the oxygenation of [Mn^{II}($dpaq^{5Cl}$)(OTf)] initially forms a mixture of (μ-oxo)dimanganese(III,III) and Mn^{III}-hydroxo species, with the latter being favored by the addition of water. In support, the energies and intensities for the electronic absorption signals for the putative [Mn^{III}(OH)($dpaq^{5Cl}$)]$^+$ species (observed upon water addition) are essentially identical to those of [Mn^{III}(OH)(dpaq)]$^+$ (Table 2.2).

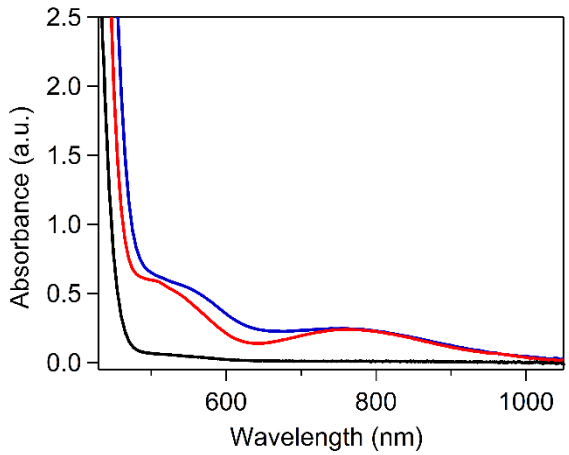

Figure 2.5 Electronic absorption spectra of [$Mn^{II}(dpaq^{5Cl})(OTf)$] before (black trace) and after (blue trace) the addition of O_2. The red trace is of the product of O_2 after addition of 560 equiv. of H_2O.

Table 2.2 Optical poroperties of Mn^{III}-hydroxo complexes supported by the $dpaq^R$ ligands.

	λ_{max} (nm)	ε_{max} ($M^{-1}cm^{-1}$)	Ep,c ($Mn^{III/II}$) vs $Cp_2Fc^{+/0}$
[a][$Mn^{III}(OH)(dpaq)]^+$	500, 770	114 (for 770 nm)	-0.73 V
[b][$Mn^{III}(OH)(dpaq^{2Me})]^+$	515, 770	228, 100	-0.62 V
[$Mn^{III}(OH)(dpaq^{5Cl})]^+$	398, 500, 770	4 240, 240, 105	-0.54 V

[a]Taken from ref. [7]

[b] Taken from ref. [8]

To provide further evidence for the assignment of a dimeric species, diffraction quality, dark brown needle like crystals of [$Mn^{III}Mn^{III}(\mu$-O)$(dpaq^{5Cl})_2](OTf)_2$ were obtained from the reaction of [$Mn^{II}(dpaq^{5Cl})(OTf)$] with 0.5 equiv. of PhIO oxidation in CH_3CN. XRD analysis of this sample revealed them to contain the (μ-oxo)dimanganese(III,III) complexes [$Mn^{III}Mn^{III}(\mu$-O$)(dpaq^{5Cl})_2](OTf)_2$ (Figure 2.6). The metric parameters for the complex, along with those predicted from previously-reported DFT computations for [$Mn^{III}Mn^{III}(\mu$-O$)(dpaq)_2]^{2+}$, are collected in Table 2.3.

***Structure and Properties of [*$\mathbf{Mn^{III}Mn^{III}(\mu}$**-O)$\mathbf{(dpaq^{5Cl})_2](OTf)_2}$ complex.** Each Mn^{III} center in [$Mn^{III}Mn^{III}(\mu$-O$)(dpaq^{5Cl})_2](OTf)_2$ is surrounded by a distorted octahedral environment with five nitrogen donors of the monoanionic $dpaq^{5Cl}$ ligand. An amide nitrogen resides at the axial position

(Figure 2.6). The two $Mn^{III}(dpaq^{5Cl})$ units are linked by a monooxo-bridged moiety with a $Mn^{III}–O–Mn^{III}$ angle of 177.78˚(Table 2.3). The almost linear angle indicates the presence of significant steric bulk encumbering the Mn centers. The strong antiferromagnetic coupling nature between the two Mn^{III} centers is further supported by the low magnetic moment of an CD_3CN solution of this complex, 1.88 μ_B. This value may also have contributions due to presence of trace amounts of $[Mn^{III}(OH)(dpaq^{5Cl})]^+$ (S = 2) species formed owing to the presence of water as impurity (37(10) ppm or 2.1(6) mM) in CD_3CN. The solid state magnetic moment of this complex, 1.18 μ_B, further supports that the dimer itself has a contribution to the μ_{eff}. This indicates that the antiferromagnetic coupling between the two Mn^{III} centers is not strong enough and that spin states above S=0 of the dimer are somewhat populated at this temperature (298 K). Both Mn^{III}–O bond distances are essentially identical in distance within error (1.797(3) Å and 1.796(3) Å) and are ~0.02 Å shorter than the corresponding distance in the monomeric species (Table 2.4). A similar shortening of bond length can be observed in the dimer for the case of Mn–N4 bond. The Mn···Mn separation is just under 3.6 Å (Table 2.3). This Mn···Mn separation is in excellent agreement with the corresponding value determined for $[Mn^{III}Mn^{III}(\mu\text{-}O)(dpaq)_2]^{2+}$ from frozen solution EXAFS data (3.55 Å).[9] In general, these metric parameters compare favorably to a series of (μ-oxo)dimanganese(III,III) complexes supported by thiolate-containing N_4S^- ligands reported by Kovacs and co-workers.[15]

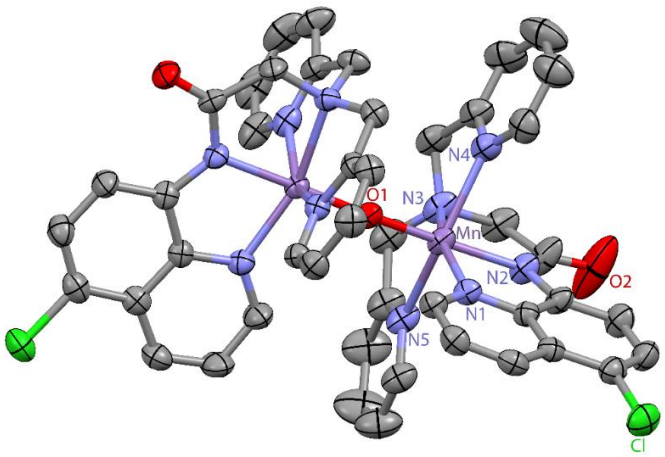

Figure 2.6 ORTEP diagrams of $[Mn^{III}Mn^{III}(\mu\text{-O})(dpaq^{5Cl})_2](OTf)_2$. Protons and triflate counter anions have been removed for clarity.

Table 2.3 Selected Manganese-Ligand Bond Lengths (Å) and Coordination Angles (°) from the Crystal Structure of $[Mn^{III}Mn^{III}(\mu\text{-O})(dpaq^{5Cl})_2](OTf)_2$ compared with corresponding distances and angles of $[Mn^{III}Mn^{III}(\mu\text{-O})(dpaq)_2]^{+}$ [9] by DFT calculations.

	$[Mn^{III}Mn^{III}(\mu\text{-O})(dpaq^{R})_2](OTf)_2$	$[Mn^{III}Mn^{III}(\mu\text{-O})(dpaq)_2]^{+}$
	R = 5Cl (q54h)	DFT
Mn–O1	1.797(3) 1.796(3)	1.81
Mn–N1	2.092(4) 2.090(4)	2.06
Mn–N2	1.985(4) 1.982(4)	1.98
Mn–N3	2.185(4) 2.183(4)	2.23
Mn–N4	2.221(4) 2.242(4)	2.35
Mn–N5	2.230(4) 2.260(5)	2.33
Mn···Mn	3.591	3.64
Mn–O1–Mn	177.78(2)	179.16

Analysis of ^{1}H NMR spectra of the $[Mn^{III}(OH)(dpaq^{5Cl})]^{+}$ and $[Mn^{III}Mn^{III}(\mu\text{-}O)(dpaq^{5Cl})_2]^{2+}$ in CD_3CN. The ^{1}H NMR spectrum (Figure 2.7) of a solution of $[Mn^{III}Mn^{III}(\mu\text{-}O)(dpaq^{5Cl})_2]^{2+}$ dissolved in CD_3CN (contains 37(10) ppm or 2.1(6) mM water as impurity) consist of peaks in the diamagnetic region (0 to 30 ppm) and low intensity hyperfine-shifted peaks in other regions (130 ppm to -30 ppm and 0 ppm to -55 ppm). These chemical shifts (in both regions) show a close resemblance to that of the previously reported spin-coupled $[Mn^{III}Mn^{III}(\mu\text{-}O)(dpaq)_2]^{2+}$ species in CD_3CN.[9] By analogy to the study performed on $[Mn^{III}Mn^{III}(\mu\text{-}O)(dpaq)_2]^{2+}$, the sharp peaks in the diamagnetic region can be assigned to the dimeric, spin-coupled $[Mn^{III}Mn^{III}(\mu\text{-}O)(dpaq^{5Cl})_2]^{2+}$ species.

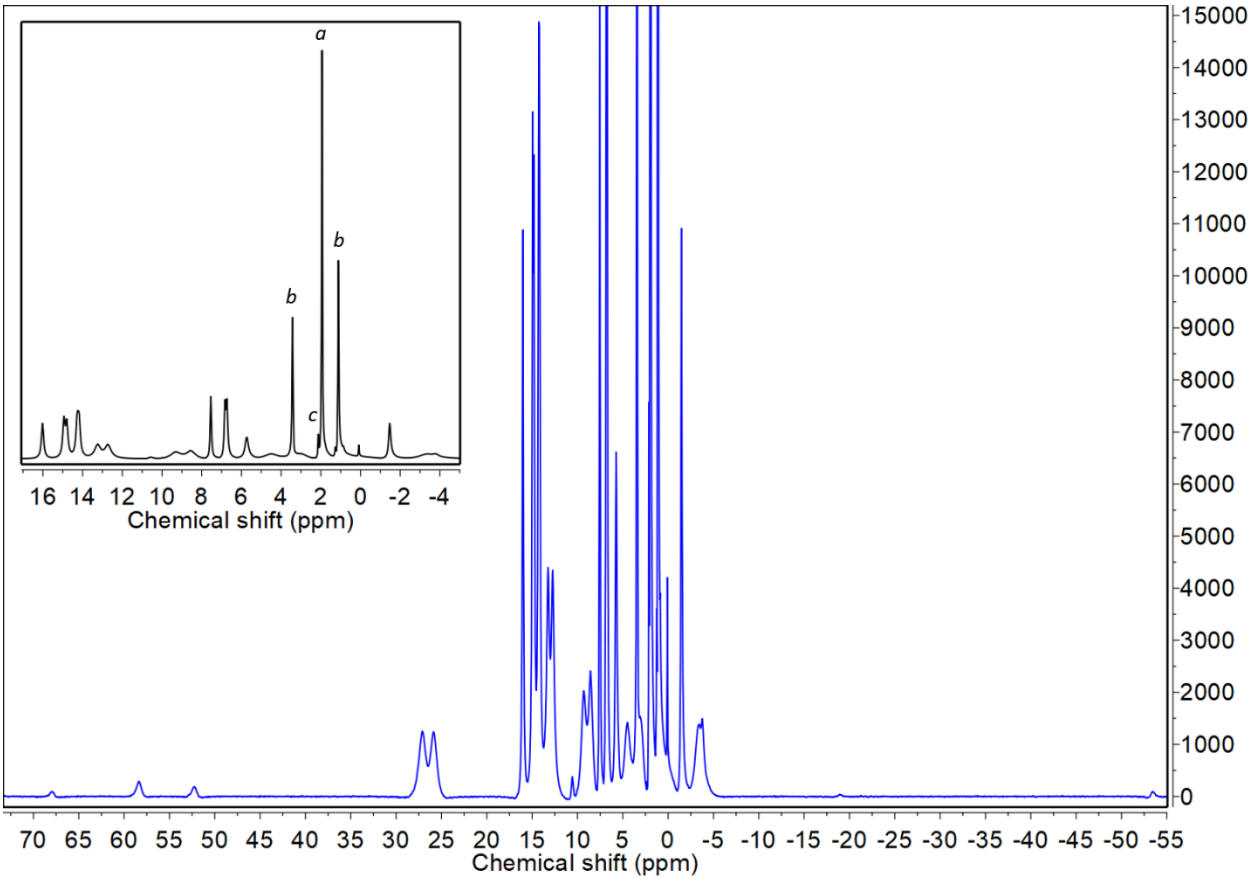

Figure 2.7 ^{1}H-NMR spectrum of spectrum of the mixture of $[Mn^{III}(OH)(dpaq^{5Cl})]^{+}$ and $[Mn^{III}Mn^{III}(\mu\text{-}O)(dpaq^{5Cl})_2]^{2+}$ (dominant species) in CD_3CN. The inset shows an expansion in the region between -4.5 and 16.5 ppm. Peaks labelled as *a, b* and *c* are due to resonances arising from acetonitrile, diethyl ether and water.

Upon addition of D_2O, the diamagnetic peaks disappear while the hyperfine-shifted peaks gain intensity (Figure 2.8). This change can be attributed to the conversion of the $[Mn^{III}Mn^{III}(\mu\text{-}O)(dpaq^{5Cl})_2]^{2+}$ species to the monomeric, S=2, $[Mn^{III}(OH)(dpaq^{5Cl})]^{+}$ species upon reacting with D_2O. Therefore the hyperfine-shifted peaks can be assigned to the product of this reaction, the $[Mn^{III}(OH)(dpaq^{5Cl})]^{+}$ species. This explanation agrees perfectly well with the previously reported ^{1}H NMR study on $[Mn^{III}(OMe)(dpaq)]^{+}$ species.[9] This conclusion is further reinforced by the X-ray diffraction analysis of crystals grown in a 90:10 (vol:vol) CH_3CN:H_2O solvent system, which was found to be of $[Mn^{III}(OH)(dpaq^{5Cl})](OTf)$. Additionally, the change in the UV-Vis profile before (blue) and after (red) addition of water (880 equiv.) to a solution containing a mixture of $[Mn^{III}Mn^{III}(\mu\text{-}O)(dpaq^{5Cl})_2]^{2+}$ and $[Mn^{III}(OH)(dpaq^{5Cl})]^{+}$ is compared in Figure 2.5.

Tentative assignment of hyperfine-shifted peaks for the $[Mn^{III}(OH)(dpaq^{5Cl})]^{+}$ species can be accomplished by comparison and rationalization of the previously reported assignments for $[Mn^{III}(OMe)(dpaq)]^{+}$ species and their peak integrations.[9] The collected values are summarized in Table 2.4. It should be noted that the ^{1}H NMR peak assignments of $[Mn^{III}(OMe)(dpaq)]^{+}$ were performed in CD_3OD while the ^{1}H NMR spectrum of $[Mn^{III}(OH)(dpaq^{5Cl})]^{+}$ was obtained in CD_3CN and therefore assignments should be carefully made as the chemical shifts values for the same protons in the two cases may show slight shifting due to solvent effects.

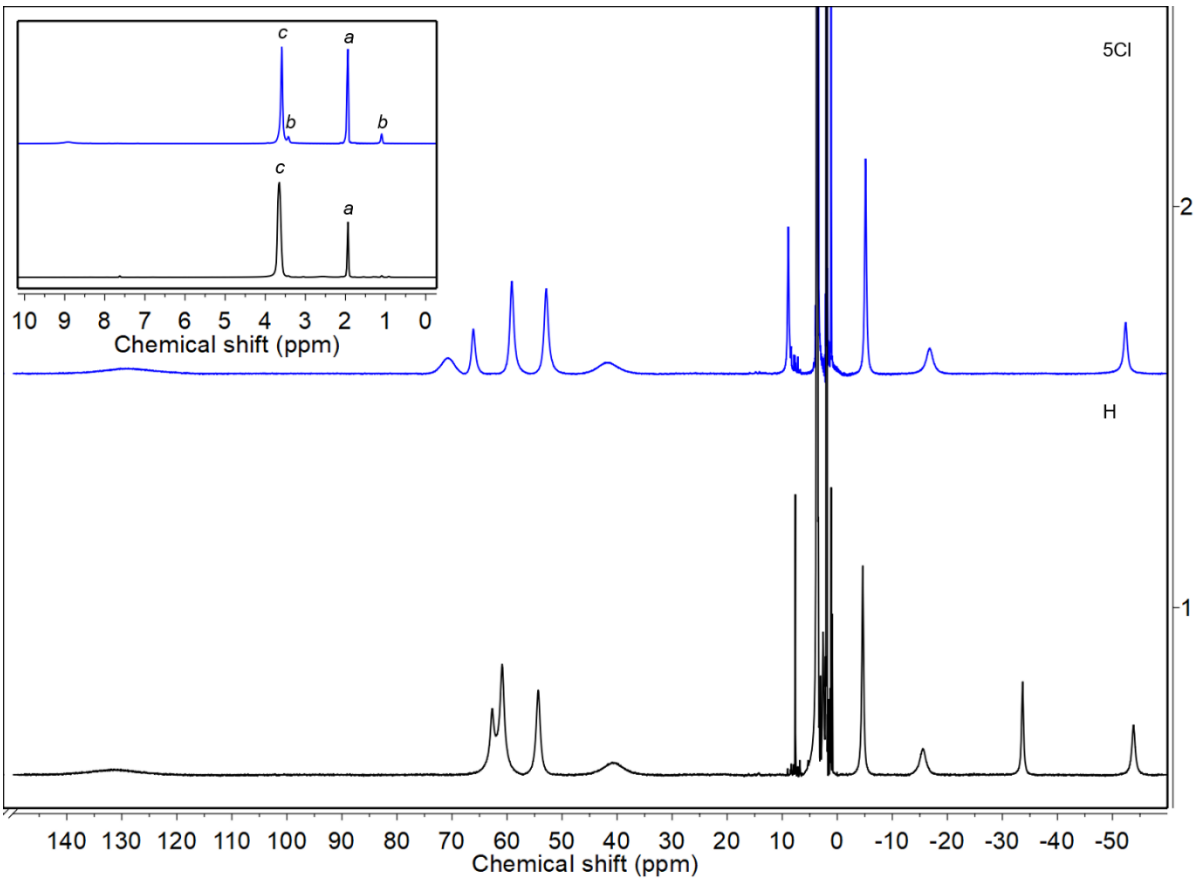

Figure 2.8 ^{1}H-NMR spectrum of spectra of $[Mn^{III}(OH)(dpaq^{5Cl})]^{+}$ after addition of water (blue trace) and $[Mn^{III}(OH)(dpaq)]^{+}$ (black trace). Both solutions have 115 µL of water added to a 500 µL, 14.5 mM (per Mn) solution of the complex in CD_3CN. The inset shows an expansion in the region between 0 and 10 ppm. Peaks labelled as *a*, *b* and *c* are due to resonances arising from acetonitrile, diethyl ether and water.

At the onset, it becomes obvious that the isolated hyperfine-shifted peak at -33.6 ppm that was tentatively assigned as a proton attached to the quinoline of $[Mn^{III}(OMe)(dpaq)]^{+}$ is not observed for the $[Mn^{III}(OH)(dpaq^{5Cl})]^{+}$ complex. The disappearance of this peak confirms the assignment of this proton as a quinoline proton and can be further deduced it as the proton at the 5th position of the quinoline. Chemical shifts observed at 127.5, 60.8, 53.9 and -4.2 ppm that were assigned as protons attached to the pyridine groups in the $[Mn^{III}(OMe)(dpaq)]^{+}$ complex show only slight shifts for the $[Mn^{III}(OH)(dpaq^{5Cl})]^{+}$ complex with perfectly agreeable peak integration

values. Minor shifts as such are expected as there is a difference in the solvent in which data were acquired although the chemical environment of the pyridine protons within the molecule are essentially identical for $[Mn^{III}(OMe)(dpaq)]^+$ and $[Mn^{III}(OH)(dpaq^{5Cl})]^+$ complexes.

The chemical shifts observed at, 59.9, 57.2, -15.7, and -52.7 ppm that were assigned as protons attached to the quinoline in the $[Mn^{III}(OMe)(dpaq)]^+$ complex show noticeable shifts for the $[Mn^{III}(OH)(dpaq^{5Cl})]^+$ complex except for the resonances at -52.7, and -15.7 ppm. The single proton peak observed at 57.2 ppm and the partially obscured, single proton broad feature observed at 59.9 ppm for the $[Mn^{III}(OMe)(dpaq)]^+$ complex have shifted downfield to manifest at 66.1 ppm and 70.7 ppm respectively for the $[Mn^{III}(OH)(dpaq^{5Cl})]^+$ complex. This makes the crowded features observed in this region for the $[Mn^{III}(OMe)(dpaq)]^+$ complex readily visible. The downfield shifts observed here arise from the electron withdrawing effect of the chloro group attached at the 5th position of quinoline. It should also be noted that the peak at 70.7 ppm still remains as a broad feature. The extremely broad feature observed at -66.3 ppm for the $[Mn^{III}(OMe)(dpaq)]^+$ complex that was assigned to the remaining proton attached to quinoline (α-H) is not observed for the $[Mn^{III}(OH)(dpaq^{5Cl})]^+$ complex at this concentration. Such loss of intensity of a resonance can be experienced for a peak like this which has an extremely short longitudinal (T_1) relaxation time.[9]

Table 2.4 ^{1}H-NMR Chemical Shifts and Peak Integrations for $[Mn^{III}(OH)(dpaq^{5Cl})]^+$, δ (ppm) acquired in CD_3CN compared with that of reported for $[Mn^{III}(OMe)(dpaq)]^+$ in CD_3OD.[9]

	$[Mn^{III}(OH)(dpaq^{5Cl})]^+$		$[Mn^{III}(OMe)(dpaq)]^+$	
	δ (ppm)	Integration	δ (ppm)	Integration
α-H (py)	128.4	2	127.5	2
H (py)	59.2	2	60.8	2
H (qn)	70.7	1	59.9[d]	1
H (qn)	66.1	1	57.2	1
H (py)	52.9	2	53.9	2

CH_2 [c]	41.7	2	38.5	2
H (py)	-5.1	2	-4.2	2
H (qn)	-16.8	2	-15.7	1
H (qn)	Not observed	_	-33.6	1
H (qn)	-52.4	1	-52.7	1
α-H (qn)	Not observed	_	-66.3	1

Structural Properties of [Mn^{III}(OH)($dpaq^{5Cl}$)](OTf) from X-ray crystallography. Crystallization of [Mn^{III}(OH)($dpaq^{5Cl}$)](OTf) was done using a modified crystal-growing protocol for [$Mn^{III}Mn^{III}$(μ-O)($dpaq^{5Cl}$)$_2$](OTf)$_2$, which involved diffusion of diethyl ether into a 90:10 (vol:vol) CH_3CN:H_2O solvent mixture at room temperature. The molecular structure of [Mn^{III}(OH)($dpaq^{5Cl}$)](OTf) shows the Mn^{III} ion in a distorted octahedral geometry, with a short Mn–O(H) distance of 1.810(2) Å (Figure 2.9 and Table 2.5). This bond length, as well as all the Mn–N distances and all coordination angles, are within error of those observed for [Mn^{III}(OH)(dpaq)]$^+$ (Table 2.5). Thus, any electronic perturbations caused by the 5-chloro-quinolinyl have no influence on the Mn^{III} coordination environment of this complex. The Mn^{III}-ligand distances of [Mn^{III}(OH)($dpaq^{5Cl}$)]$^+$ are altered compared to [Mn^{III}(OH)($dpaq^{2Me}$)]$^+$, with the major changes being the elongated Mn–N(quinolinyl) and Mn–N(amine) distances and shortened Mn–N(pyridyl) distances of the latter complex (Table 2.5). It should also be noted that the Mn–N(amide) bond length, 1.976(2) Å of [Mn^{III}(OH)($dpaq^{5Cl}$)]$^+$ is slightly longer than that of observed by Hitomi for the [Mn(NO)($dpaq^{5Cl}$)]$^+$ complex (1.941(3) Å).[13]

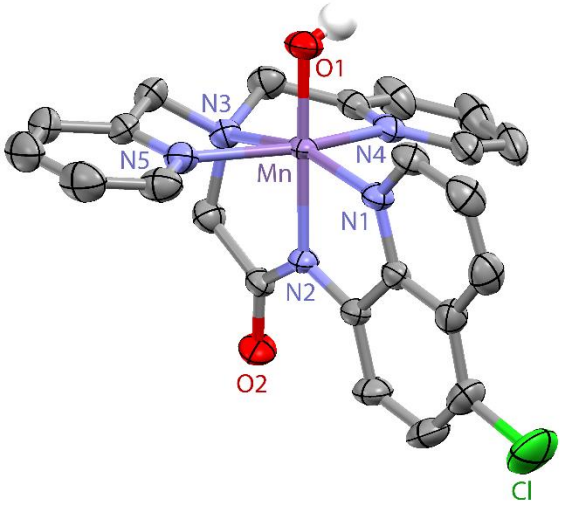

Figure 2.9 ORTEP diagram of [Mn^{III}(OH)dpaq^{5Cl})](OTf). Protons and triflate counter anion have been removed for clarity.

Table 2.5 Selected Manganese-Ligand Bond Lengths (Å) and Coordination Angles (°) from the Crystal Structures of [Mn^{III}(OH)(dpaq^{5Cl})](OTf), [Mn^{III}(OH)(dpaq)](OTf),[7] and [Mn^{III}(OH)(dpaq^{2Me})](OTf).[8]

	[Mn^{III}(OH)(dpaq^{R})](OTf)		
	R = 5Cl	R = H	R = 2Me
Mn–O1	1.810(2)	1.806(13)	1.819(3)
Mn–N1	2.066(2)	2.072(14)	2.186(3)
Mn–N2	1.976(2)	1.975(14)	1.979(3)
Mn–N3	2.167(2)	2.173(14)	2.203(3)
Mn–N4	2.245(2)	2.260(14)	2.148(3)
Mn–N5	2.218(2)	2.216(15)	2.158(3)
N2–Mn^{III}–O1	178.35(8)˚	177.94(6)˚	174.45˚
N4–Mn^{III}–N5	153.18(8)˚	152.53(5)˚	155.18˚
N1–Mn^{III}–N3	162.35(8)˚	161.83(6)˚	160.78˚
N4–Mn^{III}–N2	85.27(7)˚	85.22(5)˚	91.69˚
N1–Mn^{III}–N2	79.63(7)˚	79.77(6)˚	79.51˚
N3–Mn^{III}–N2	82.74(8)˚	82.51(6)˚	81.54˚

Cyclic Voltammetry of [Mn^{III}(OH)dpaq^{5Cl})](OTf). Cyclic voltammetry (CV) experiments were performed for the [Mn^{III}(OH)dpaq^{5Cl})](OTf) complex in a 10 mL of 98:2 (vol:vol) CH_3CN:H_2O solvent mixture. An irreversible reduction response was observed at -0.54 V (vs Fc^+/Fc) that is attributed to the $Mn^{III/II}$ couple. Comparison of previously reported potentials of [Mn^{III}(OH)(dpaq^{R})]$^+$ derivatives show that values increase in the order of [Mn^{III}(OH)(dpaq)]$^+$ (-0.73 V)[8] < [Mn^{III}(OH)(dpaq^{2Me})]$^+$ (-0.62 V)[8] < [Mn^{III}(OH)(dpaq^{5Cl})]$^+$ (-0.54 V, this study).

TEMPOH Oxidation by Mn^{III}-hydroxo Complex. The HAT reactivity of the [Mn^{III}(OH)(dpaq^{5Cl})]$^+$ complex was assessed using TEMPOH. The experiments were performed in a solvent mixture of 98:2 (vol:vol) CH_3CN:H_2O, which ensures that the Mn^{III}-hydroxo species is dominant in solution. In these experiments, an excess of TEMPOH (10 – 40 equivalents) was added to the [Mn^{III}(OH)(dpaq^{5Cl})]$^+$ complex at -35 °C, which resulted in the disappearance of the characteristic optical bands of the Mn^{III}-hydroxo species (Figure 2.10 left). Under these conditions, each decay followed first order behavior to at least five half-lives, permitting the determination of pseudo-first order rate constants (k_{obs}).

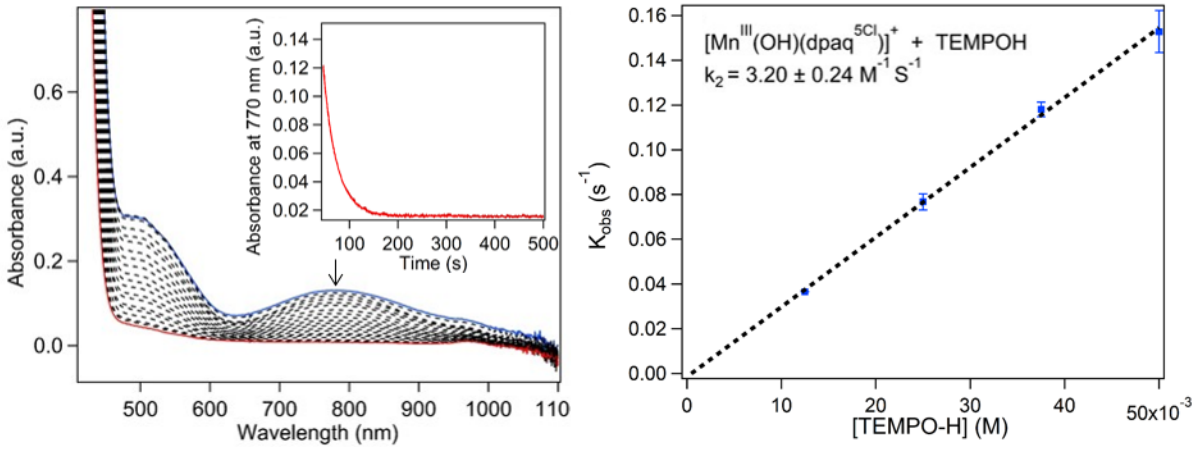

Figure 2.10 Disappearance of the characteristic optical bands of $[Mn^{III}(OH)(dpaq^{5Cl})]^+$ upon addition of TEMPOH (left). Pseudo first order rate constants k_{obs} (s^{-1}) as a function TEMPOH concentration (right). The second-order rate constant k_2 was calculated from the slope.

Second-order rate constant (k_2) for the reaction was obtained by fitting the increase in k_{obs} vs TEMPOH concentration to a linear function (Figure 2.10 right). The second-order rate constants obtained for the $[Mn^{III}(OH)(dpaq^{5Cl})]^+$ complex is given in Table 2.6 along with k_2 values previously reported for the $[Mn^{III}(OH)(dpaq)]^+$ and $[Mn^{III}(OH)(dpaq^{2Me})]^+$ for comparison. These data show an increase in k_2 in the following order $[Mn^{III}(OH)(dpaq^{5Cl})]^+$ ~ $[Mn^{III}(OH)(dpaq^{2Me})]^+$ > $[Mn^{III}(OH)(dpaq^{H})]^+$.

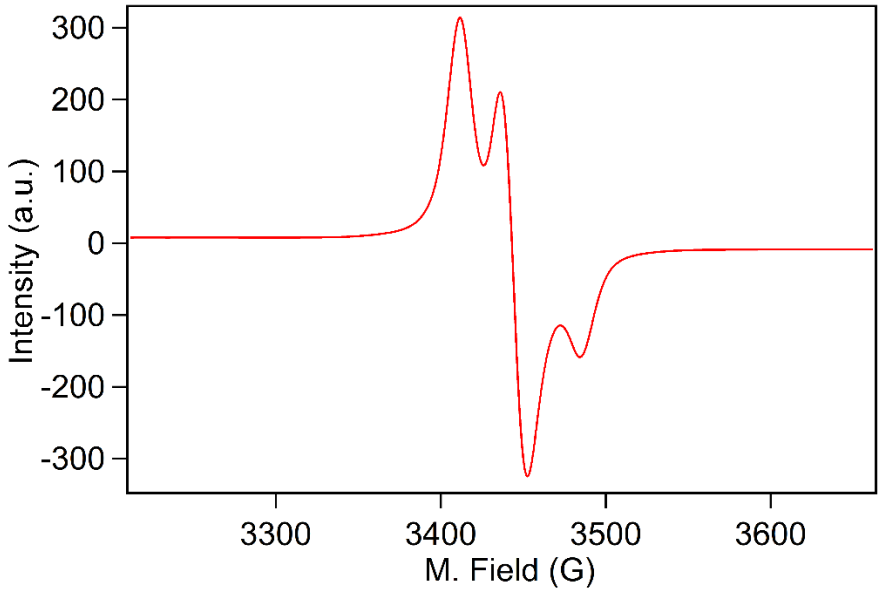

Figure 2.11 Perpendicular-mode X-band EPR spectrum of the final product of reaction of 1.25 mM $[Mn^{II}(dpaq^{5Cl})(OTf)]$ with 20 equiv. of TEMPOH prepared in 98:2 (vol:vol) $CH_3CN:H_2O$ measured at 5 K.

Table 2.6 Second Order Rate Constants of Mn^{III}-hydroxo Complexes Supported by the $dpaq^R$ Ligands.

	TEMPOH k_2 ($M^{-1}s^{-1}$)
$[Mn^{III}(OH)(dpaq)]^{+a}$	1.1(1)
$[Mn^{III}(OH)(dpaq^{2Me})]^{+b}$	3.1(3)

$[Mn^{III}(OH)(dpaq^{5Cl})]^{+}$	3.2(2)

[a] Collected from ref. [7]

[b] Collected from ref. [8]

The perpendicular-mode X-band EPR spectrum of the final reaction mixture of the reaction of $[Mn^{III}(OH)(dpaq^{5Cl})]^{+}$ with 20 equiv. of TEMPOH measured at 5 K depicts a sharp feature centered at g = 2.03 that can attributed for the TEMPO radical species in CH_3CN (Figure 2.11).

2.4 Conclusions

In this study we introduce a new addition to the series of Mn-dpaq complexes which include the characterization of the following species: $[Mn^{II}(dpaq^{5Cl})(OTf)]$, $[Mn^{III}(OH)(dpaq^{5Cl})](OTf)$ and $[Mn^{III}Mn^{III}(\mu\text{-}O)(dpaq^{5R})_2](OTf)$. The structure of $[Mn^{II}(dpaq^{5Cl})(OTf)]$ analyzed by X-ray diffraction studies gives the first example of structural characterization of a Mn^{II}-$dpaq^{5R}$ species. This structure has a monomeric form as opposed to the polymeric structures previously reported for $[Mn^{II}(dpaq^{2Me})](OTf)$[8] and $[Mn^{II}(dpaq)](OTf)$ complexes.[7] Oxidation of $[Mn^{II}(dpaq)](OTf)$ by O_2 or PhIO resulted in an equilibrium mixture of a mononuclear Mn^{III}-hydroxo and a spin-coupled dinuclear species in MeCN solution. Presence of a mixture as mentioned above was further confirmed by both ^1H NMR and electronic absorption methods, where it was shown that addition of water converts the majority of dimer species into the monomer species. X-ray diffraction analysis of crystalline $[Mn^{III}(OH)(dpaq^{5Cl})](OTf)$ grown in a wet CH_3CN solvent system revealed an intermediate Mn^{III}–OH bond distance when compared to that of $[Mn^{III}(OH)(dpaq^{2Me})](OTf)$[8] and $[Mn^{III}(OH)(dpaq)](OTf)$. This complex participates in HAT reactivity via oxidation of TEMPOH at -35 ˚C with a the second order rate constant that is almost identical to that of $[Mn^{II}(dpaq^{2Me})](OTf)$. X-ray diffraction studies of crystalline $[Mn^{III}Mn^{III}(\mu\text{-}O)(dpaq^{5R})_2](OTf)$

prepared by PhIO oxidation of [Mn^{II}($dpaq^{5Cl}$)(OTf)] in dry CH_3CN provides further evidence for presence of a spin-coupled dinuclear species in the above mentioned mixture.

2.5 References

1. Mayer, J. M., Understanding Hydrogen Atom Transfer: From Bond Strengths to Marcus Theory. *Accounts of Chemical Research* **2011,** *44* (1), 36-46.

2. Warren, J. J.; Tronic, T. A.; Mayer, J. M., Thermochemistry of Proton-Coupled Electron Transfer Reagents and its Implications. *Chemical Reviews* **2010,** *110* (12), 6961-7001.

3. Su, C.; Sahlin, M.; Oliw, E. H., Kinetics of Manganese Lipoxygenase with a Catalytic Mononuclear Redox Center. *Journal of Biological Chemistry* **2000,** *275* (25), 18830-18835.

4. Gao, H.; Groves, J. T., Fast Hydrogen Atom Abstraction by a Hydroxo Iron(III) Porphyrazine. *Journal of the American Chemical Society* **2017,** *139* (11), 3938-3941.

5. Goldsmith, C. R.; Cole, A. P.; Stack, T. D. P., C−H Activation by a Mononuclear Manganese(III) Hydroxide Complex: Synthesis and Characterization of a Manganese-Lipoxygenase Mimic? *Journal of the American Chemical Society* **2005,** *127* (27), 9904-9912.

6. Coggins, M. K.; Brines, L. M.; Kovacs, J. A., Synthesis and Structural Characterization of a Series of MnIIIOR Complexes, Including a Water-Soluble MnIIIOH That Promotes Aerobic Hydrogen-Atom Transfer. *Inorganic Chemistry* **2013,** *52* (21), 12383-12393.

7. Wijeratne, G. B.; Corzine, B.; Day, V. W.; Jackson, T. A., Saturation Kinetics in Phenolic O–H Bond Oxidation by a Mononuclear Mn(III)–OH Complex Derived from Dioxygen. *Inorganic Chemistry* **2014,** *53* (14), 7622-7634.

8. Rice, D. B.; Wijeratne, G. B.; Burr, A. D.; Parham, J. D.; Day, V. W.; Jackson, T. A., Steric and Electronic Influence on Proton-Coupled Electron-Transfer Reactivity of a Mononuclear Mn(III)-Hydroxo Complex. *Inorganic Chemistry* **2016,** *55* (16), 8110-8120.

9. Rice, D. B.; Jones, S. D.; Douglas, J. T.; Jackson, T. A., NMR Studies of a MnIII-hydroxo Adduct Reveal an Equilibrium between MnIII-hydroxo and μ-Oxodimanganese(III,III) Species. *Inorganic Chemistry* **2018,** *57* (13), 7825-7837.

10. Hitomi, Y.; Arakawa, K.; Kodera, M., Electronic Tuning of Iron-Oxo-Mediated C□H Activation: Effect of Electron-Donating Ligand on Selectivity. *Chemistry - A European Journal* **2013,** *19* (43), 14697-14701.

11. Riedel, P. J.; Arulsamy, N.; Mehn, M. P., Facile routes to manganese(II) triflate complexes. *Inorganic Chemistry Communications* **2011,** *14* (5), 734-737.

12. Mader, E. A.; Davidson, E. R.; Mayer, J. M., Large Ground-State Entropy Changes for Hydrogen Atom Transfer Reactions of Iron Complexes. *Journal of the American Chemical Society* **2007,** *129* (16), 5153-5166.

13. Hitomi, Y.; Iwamoto, Y.; Kodera, M., Electronic tuning of nitric oxide release from manganese nitrosyl complexes by visible light irradiation: enhancement of nitric oxide release efficiency by the nitro-substituted quinoline ligand. *Dalton Trans.* **2014,** *43* (5), 2161-2167.

14. Pavlishchuk, V. V.; Addison, A. W., Conversion constants for redox potentials measured versus different reference electrodes in acetonitrile solutions at 25°C. *Inorganica Chimica Acta* **2000,** *298* (1), 97-102.

15. Coggins, M. K.; Toledo, S.; Shaffer, E.; Kaminsky, W.; Shearer, J.; Kovacs, J. A., Characterization and Dioxygen Reactivity of a New Series of Coordinatively Unsaturated Thiolate-Ligated Manganese(II) Complexes. *Inorganic Chemistry* **2012,** *51* (12), 6633-6644.

Chapter 3: Thermodynamics of a series of Mn^{III}-OH complexes that can participate in hydrogen atom transfer reactions

3.1 Introduction

Hydrogen atom transfer (HAT) reactions are fundamental reactions in heme and nonheme metalloenzymes and synthetic transition metal chemistry. Especially in nature, these reactions play important roles from transfer of energy to the chemistry of reactive oxygen species and antioxidants in metalloenzymes.[1] Understanding HAT reactions of metalloenzymatic reactions are crucial in utilizing their high efficiency and selectivity in synthetic chemistry. Several different approaches have been taken over the past few decades to describe HAT reactivity that include the use of Bell-Evans-Polanyi plots, the Bordwell equation, Van't Hoff plots and Marcus cross relation.[2-7] This study will focus more on using the Bordwell equation (Equation 3.1) to determine the driving force of the HAT reactions.

$$\boldsymbol{BDFE_{solv}(X-H) = 1.37pK_a + 23.06E^0 + C_{G,sol}} \qquad 3.1$$

Understanding of the HAT reactivity of metal-oxo and metal-hydroxo complexes is greatly aided by the thermodynamics of the hydrogen-atom abstracting ability of the oxidant. In the past few decades, with nature as inspiration, high valent metal-oxo complexes have shown promising reactivity in HAT reactions and their reactivity has been well studied. These mainly include oxoiron(IV), oxomanganese(IV) and oxoruthenium(IV) complexes that can oxidize weak and strong C–H or O–H bonds.[8-11] In contrast, studies on thermodynamics of biomimetic low and mid valent metal-hydroxo complexes that participate in HAT reactivity are less explored.[4-5]

For a HAT reaction by a Mn^{III}-hydroxo adduct, the thermodynamic driving force of the reaction is derived from the difference between the BDFE of the O–H bond formed in the Mn^{II}-aqua product and the BDFE of the substrate C–H (or O–H) bond under attack. Experimental BDFEs for a broad range of substrates have been tabulated,[12] and there are validated computational approaches for determining BDFEs as well.[10, 13] The following studies have been carried out with

the inspiration of Mn-lipoxygenase active site and its reactivity with polyunsaturated fatty acid substrates with weak C–H bonds. For example, for a Mn^{II}-aqua complex, a BDFE for $[Mn^{II}(OH_2)(S^{Me2}N_4(tren))]^+$ was determined electrochemically, by measuring the reduction ($E_{p,c}$) of the Mn^{III}-hydroxo complex as a function of pH, and a BDFE for $[Mn^{II}(OH_2)(PY5)]^+$ was determined using a thermodynamic cycle involving the independently measured $Mn^{III/II}$ peak potential and Mn^{II}-aqua p*Ka* value. The substantially stronger O–H BDFE of $[Mn^{II}(OH_2)(PY5)]^{2+}$ (82 kcal/mol in MeCN) compared to $[Mn^{II}(OH_2)(S^{Me2}N_4(tren))]^+$ (70.1 kcal/mol in MeCN) is consistent with the greater HAT abilities of the former complex. While intermediate BDFE values would be anticipated for the $[Mn^{III}(OH)(dpaq)]^+$ and $[Mn^{III}(OH)(dpaq^{2Me})]^+$ complexes introduced in chapter 2, a complete thermodynamic description has not yet been reported.

The above four complexes discussed that were developed with lipoxygenase as inspiration, undergo HAT reactivity with H atom donors such as TEMPOH. It should be noted that the second order rate constants for the reaction with TEMPOH, display an anomaly when comparing the corresponding reported values for $[Mn^{III}(OH)(S^{Me2}N_4(tren))]^+$ (2.1×10^3 $M^{-1}s^{-1}$, 298 K)[5] and $[Mn^{III}(OH)(dpaq^{2Me})]^+$ (k_2 = 31 $M^{-1}s^{-1}$, 298 K)[14] complexes. This is an incongruity because the estimated O–H BDFE of $[Mn^{II}(OH_2)(S^{Me2}N_4(tren))]^+$, 70.1 kcal mol^{-1} is almost identical to that of the predicted corresponding value for $[Mn^{II}(H_2O)(dpaq^{2Me})]^+$, 69.2 kcal mol^{-1}.[5, 14] This anomaly can be potentially attributed to the differences in the coordinating atoms and steric bulk around the Mn^{III} center.

Through comparison of above four lipoxygenase mimics, it is evident that minor differences in the geometric and electronic structure of the Mn^{III}–OH moiety can alter the reactivity significantly. Thus more synthetic models are required to confidently describe the HAT reactivity of Mn-LOX. The objective of this study is to extend the previously reported $[Mn^{III}(OH)(dpaq)]^+$

and $[Mn^{III}(OH)(dpaq^{2Me})]^+$ series with the $[Mn^{III}(OH)(dpaq^{5Cl})]^+$ complex and determine the thermodynamic parameters that govern the HAT reactivity of these complexes.

3.2 Materials and Methods.

3.2.1 Generation of $[Mn^{II}(OH_2)(dpaq)]+$, $[Mn^{II}(OH_2)(dpaq^{2Me})]^+$, $[Mn^{II}(OH_2)(dpaq^{5Cl})]+$, $[Mn^{II}(OH_2)(dpaq^{5MeO})]^+$ Complexes. A 3 mL solution of 0.125 mM $[Mn^{II}(dpaq^{R})](OTf)$ (where $dpaq^{R}$ = dpaq, $dpaq^{2Me}$, $dpaq^{5MeO}$ and $dpaq^{5Cl}$) in CH_3CN was treated with 100 μL aliquots of Milli-Q Ultra-pure H_2O under an Ar(g) atmosphere, while continuously monitoring the reaction by electronic absorption spectroscopy. Additions of 100 μL aliquots of water were continued until no further significant changes were observed in the position of the respective characteristic high energy bands of the $[Mn^{II}(dpaq^{R})]^+$ complexes. In this process, the UV-Vis band of $[Mn^{II}(dpaq^{5Cl})]^+$ shows an isosbestic point at a wavelength of 370 nm (Figure 3.1) Further addition of water to a $[Mn^{II}(dpaq^{5Cl})]^+$ solution at 92: 8 (vol:vol) $CH_3CN:H_2O$ results in comparatively smaller shifts in the peak maximum (375 nm) to higher energy.

3.2.3 Kinetic Studies of TEMPOH oxidation by $[Mn^{III}(OH)(dpaq^{5Cl})](OTf)$. Kinetic experiments were carried by following an analogous procedure as described in section 2.3. The reactions were carried out at -10 ˚C instead of -35 ˚C and used a 90:10 (vol:vol) $CH_3CN:H_2O$ solvent system instead of a 98:2 (vol:vol) $CH_3CN:H_2O$. Solutions of $[Mn^{III}(OH)(dpaq^{5Cl})](OTf)$ with concentrations of 1.25 mM and 0.125 mM of were used in studying kinetics with TEMPOH.

3.2.4 Cyclic Voltammetry for $[Mn^{III}(OH)(dpaq^{R})](OTf)$. Cyclic voltammetry (CV) data were collected for 1.0 mM solutions of $[Mn^{III}(OH)(dpaq^{R}](OTf)$ (where $dpaq^{R}$ = dpaq, $dpaq^{2Me}$, and $dpaq^{5Cl}$) in 90:10 (vol:vol) $CH_3CN:H_2O$. All CV experiments were performed under an inert atmosphere. Solvents were purged with nitrogen to remove oxygen until no redox peaks related to oxygen were observed. A Ag/AgCl quasi-reference electrode, a platinum auxiliary electrode, and

a glassy carbon electrode were used as the three electrode system, with 0.1 M $Bu_4N(PF_6)$ as the supporting electrolyte. Peak positions were referenced to the Fc^+/Fc couple, which was collected under identical experimental conditions. Conversion of the Fc^+/Fc potential in CH_3CN to SCE employed a correction of +0.38 V.[15]

3.3 Results and Analysis.

Thermodynamic Analysis of Hydrogen-Atom Transfer by Mn^{III}-hydroxo Complexes. To better understand the reactivity of these Mn^{III}-hydroxo complexes with TEMPOH, we performed CV to determine the $Mn^{III/II}$ reduction potentials of the respective complexes. The corresponding Mn^{II}-H_2O complexes were prepared with the intention of aiding future studies of p*Ka* analysis using acid-base titrations.

Comparison of Products Formed from the Reaction of $[Mn^{III}(OH)(dpaq^{5Cl})](OTf)$ with excess TEMPOH in 98:2 (vol:vol) CH_3CN:H_2O and 90:10 (vol:vol) CH_3CN:H_2O solvent systems. The $[Mn^{III}(OH)(dpaq^{5Cl})](OTf)$ complex, as mentioned previously has a sharp UV-Vis feature at 398 nm in 98:2 (vol:vol) CH_3CN:H_2O solvent system. Upon addition of excess TMEPOH (10 equiv.) to this solution, the growth of a new UV-Vis feature at 386 nm is observed (Figure 3.1). Figure 3.2 left, shows the increase of absorbance of the peak at 386 nm with respect to time just after addition of TEMPOH. This new feature at 386 nm closely resembles that of $[Mn^{II}(dpaq^{5Cl})(OTf)]$ dissolved in a 98:2 (vol:vol) CH_3CN:H_2O solvent system (Figure 3.2, right). In both cases, the dominant species is the $[Mn^{II}(NCMe)(dpaq^{5Cl})]^+$ species in solution while the $[Mn^{II}(OH_2)(dpaq^{5Cl})]^+$ will be present as the minor product due to the presence of 2% of H_2O (v/v %) in solution. A descriptive analysis of generation of Mn^{II}–OH_2 complexes and spectral changes resulting due to addition of water are discussed in the next section. Figures 3.3 and 3.4 show that in 90:10 (vol:vol) CH_3CN:H_2O solvent system the final UV-Vis profile of reaction of

$[Mn^{III}(OH)(dpaq^{5Cl})](OTf)$ with excess TEMPOH compares well with that of $[Mn^{II}(OH_2)(dpaq^{5Cl})]^+$ measured in 90:10 (vol:vol) $CH_3CN:H_2O$ solvent system.

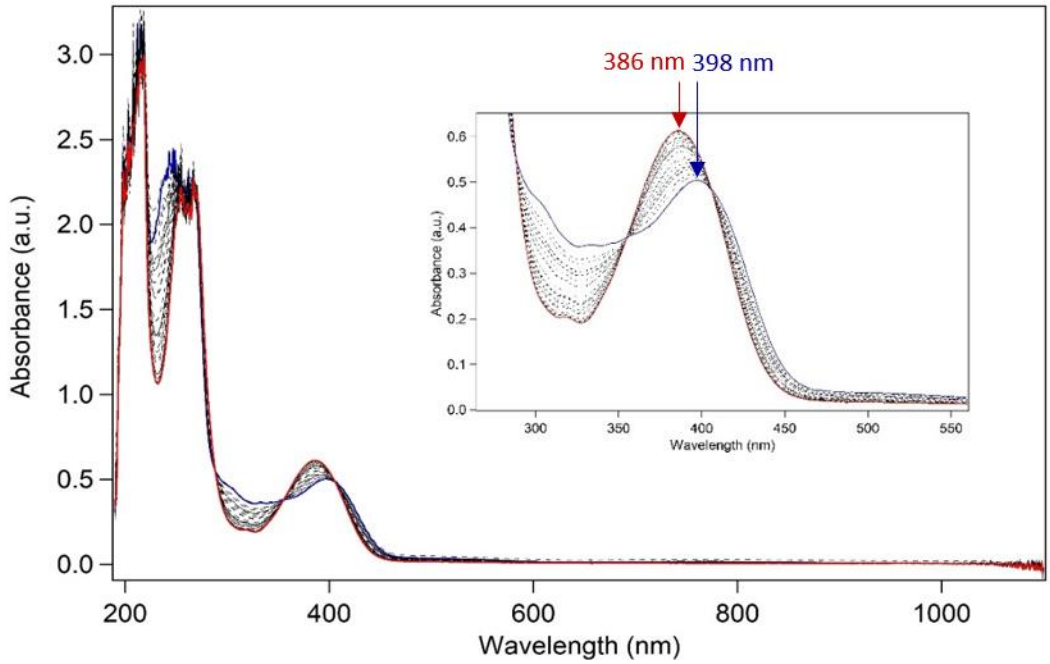

Figure 3.1 UV-Vis spectral changes during reaction of $[Mn^{III}(OH)(dpaq^{5Cl})](OTf)$ with excess TEMPOH in 98:2 (vol:vol) $CH_3CN:H_2O$ solvent system. Blue trace: $[Mn^{III}(OH)(dpaq^{5Cl})](OTf)$, Red trace: Product.

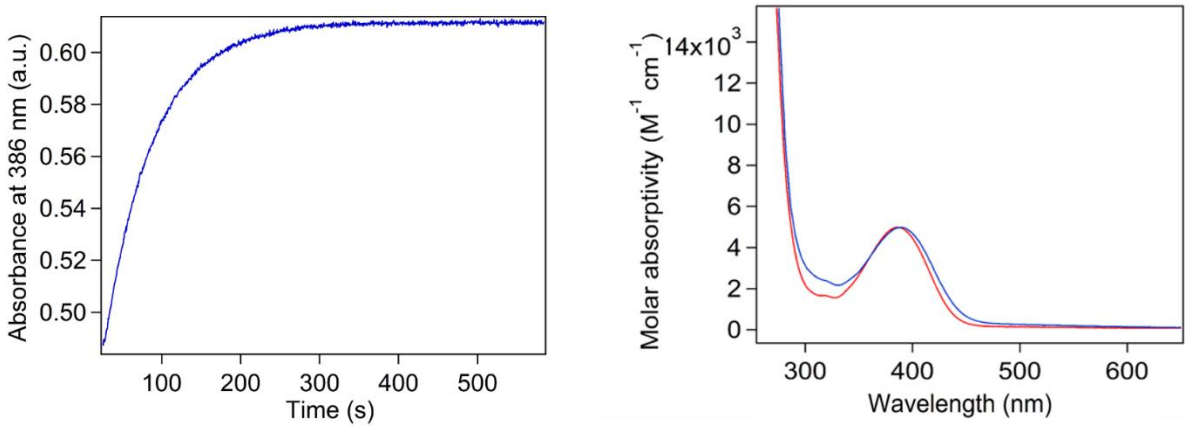

Figure 3.2 Behavior of absorbance at 386 nm upon addition of excess of TEMPOH to $[Mn^{III}(OH)(dpaq^{5Cl})](OTf)$ in 98:2 (vol:vol) $CH_3CN:H_2O$ solvent system at -10 C˚ (Left Figure). Comparison of product of reaction of $[Mn^{III}(OH)(dpaq^{5Cl})](OTf)$ with TEMPOH and $[Mn^{II}(NCCH_3)(dpaq^{5Cl})]^+$ in 98:2 (vol:vol) $CH_3CN:H_2O$ solvent system.

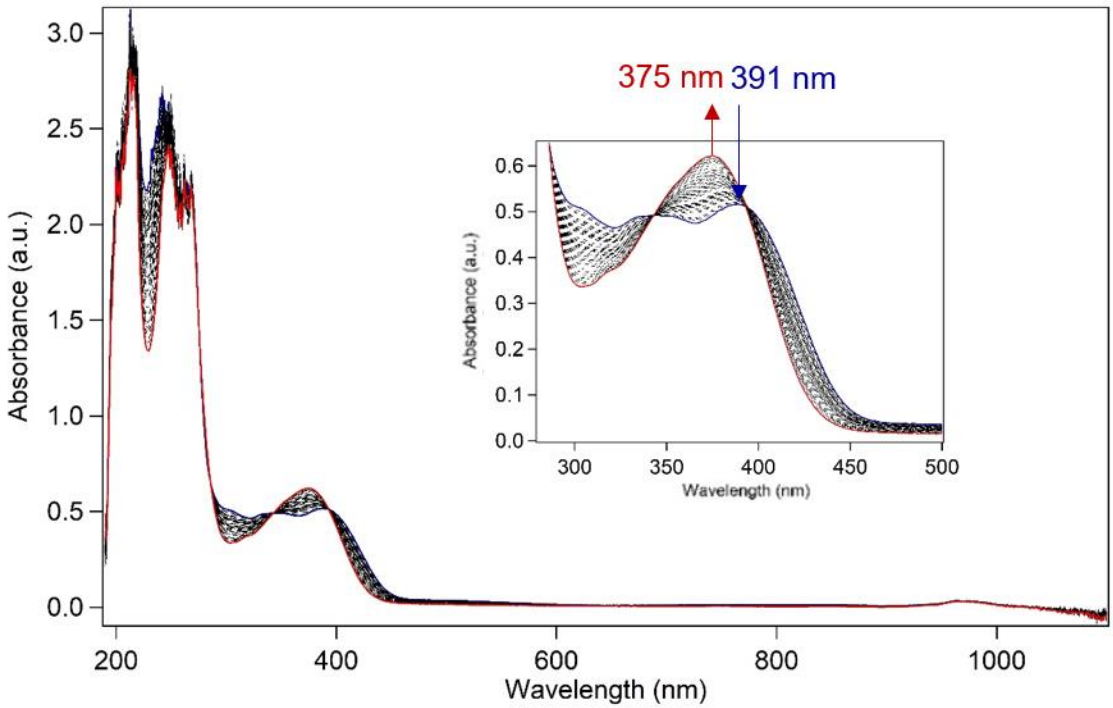

Figure 3.3 UV-Vis spectral changes during reaction of $[Mn^{III}(OH)(dpaq^{5Cl})](OTf)$ with excess TEMPOH in 90:10 (vol:vol) $CH_3CN:H_2O$ solvent system. Blue trace: $[Mn^{III}(OH)(dpaq^{5Cl})](OTf)$, Red trace: Product.

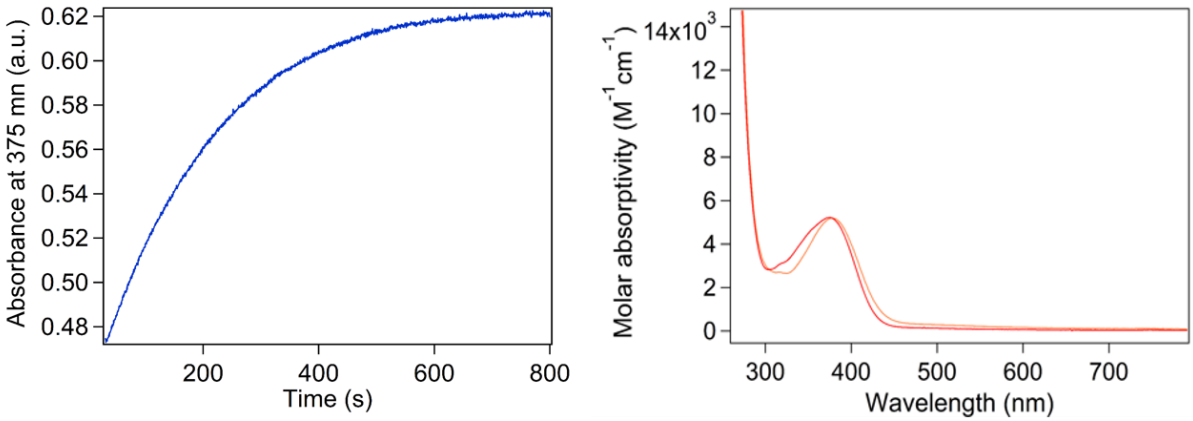

Figure 3.4 Left Figure: Behavior of absorbance at 375 nm upon addition of excess of TEMPOH to $[Mn^{III}(OH)(dpaq^{5Cl})](OTf)$ in 90:10 (vol:vol) $CH_3CN:H_2O$ solvent system at -10 C˚. Right

Figure: Comparison of product of reaction of $[Mn^{III}(OH)(dpaq^{5Cl})](OTf)$ with TEMPOH and $[Mn^{II}(NCCH_3)(dpaq^{5Cl})]^+$ in 90:10 (vol:vol) $CH_3CN:H_2O$ solvent system.

Generation of Mn^{II}-Aqua Complexes. The Mn^{II}-aqua complexes of the $dpaq^R$ ligands were generated by adding 100 µL aliquots of H_2O to CH_3CN solutions of 0.125 mM $[Mn^{II}(dpaq^R)](OTf)$ at 25 °C. The low concentration of Mn^{II} complex allowed us to follow changes in the UV region of the electronic absorption spectrum upon H_2O addition. Using $[Mn^{II}(dpaq^{5Cl})(OTf)]$ as a representative example, this complex shows a characteristic electronic absorption band at 388 nm when dissolved in CH_3CN. The addition of 100 µL aliquots of H_2O to this complex resulted in a loss of absorption intensity at 388 nm and the appearance of a band at 375 nm with isosbestic points at 370 nm and 298 nm (Figure 3.5).

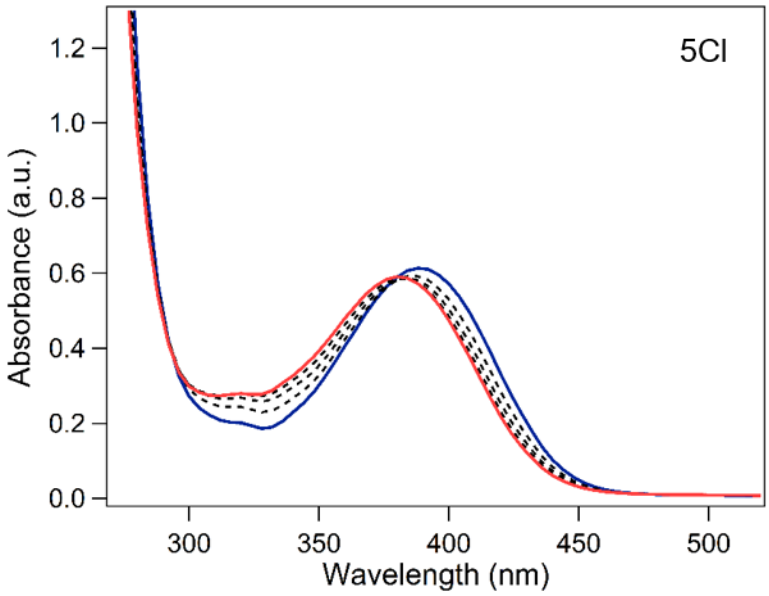

Figure 3.5 Change in the electronic absorption spectrum upon addition of 100 µL aliquots of water to $[Mn^{II}(dpaq^{5Cl})]^+$ solution in CH_3CN.

The reaction was complete with the addition of 8% H_2O by volume. This conversion was reversible, as the addition of CH_3CN to a 92:8 (vol:vol) $CH_3CN:H_2O$ solution of

[Mn^{II}(dpaq^{5Cl})(OTf)] caused a loss of absorption intensity at 375 nm and the concomitant growth of the band at 388 nm. These data suggest that the addition of a sufficient quantity of water causes a reversible conversion from [Mn^{II}(NCMe)(dpaq^{5Cl})]$^{+}$ to [Mn^{II}(OH_2)(dpaq^{5Cl})]$^{+}$.

Similar spectral changes were observed when the [Mn^{II}(dpaq)](OTf) and [Mn^{II}(dpaq^{2Me})](OTf) complexes were dissolved in CH_3CN and aliquots of H_2O were added to these solutions (Figures 3.6 and 3.7). In each case, the addition of water caused an electronic absorption band in the UV to shift to higher energy. In contrast, experiments performed on [Mn^{II}(dpaq^{5NO2})](OTf) following the same procedure did not result in any significant peak shifting (Figure 3.8).

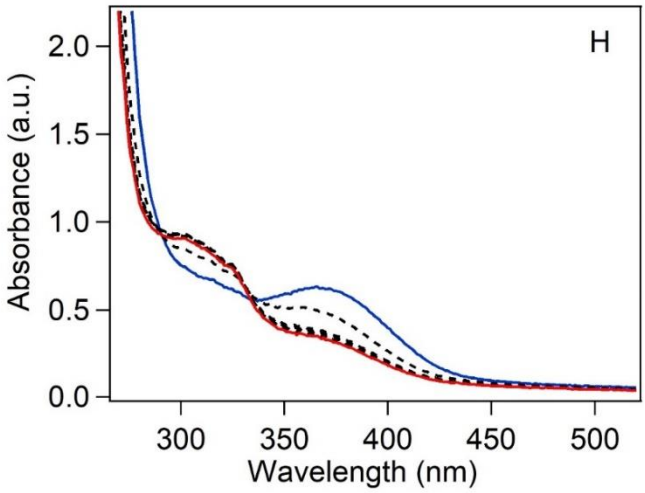

Figure 3.6 Change in the electronic absorption spectrum upon addition of 100 μL aliquots of water to [Mn^{II}(dpaq)]$^{+}$ solution in CH_3CN.

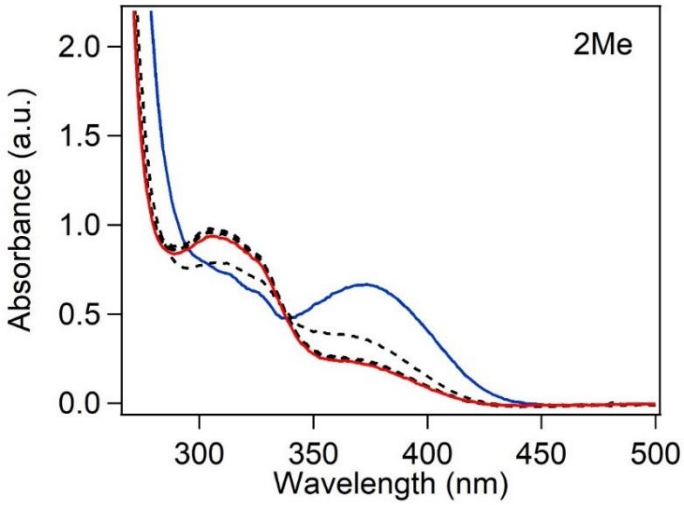

Figure 3.7 Change in the electronic absorption spectrum upon addition of 100 μL aliquots of water to $[Mn^{II}(dpaq^{2Me})]^{+}$ solution in CH_3CN.

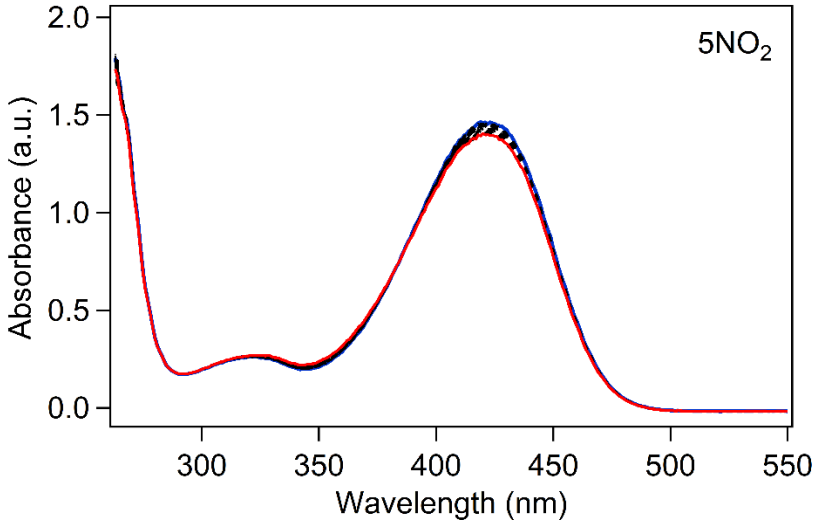

Figure 3.8 Change in the electronic absorption spectrum upon addition of 100 μL aliquots of water to $[Mn^{II}(dpaq^{5NO2})]^{+}$ solution in CH_3CN.

Cyclic Voltammetry of [Mn^{III}(OH)dpaq)](OTf), [Mn^{III}(OH)$dpaq^{2Me}$)](OTf), and [Mn^{III}(OH)$dpaq^{5Cl}$)](OTf) Complexes. Cyclic voltammetry (CV) experiments were performed for the $[Mn^{III}(OH)dpaq^{R})](OTf)$ complexes in a 10 mL of 90:10 (vol:vol) $CH_3CN:H_2O$ solvent

mixture. Irreversible reduction responses were observed for each complex that is attributed to the $Mn^{III/II}$ couple. The potentials increase in the order of $[Mn^{III}(OH)(dpaq)]^{+}$ (-0.70 V) < $[Mn^{III}(OH)(dpaq^{2Me})]^{+}$ (-0.63 V) < $[Mn^{III}(OH)(dpaq^{5Cl})]^{+}$ (-0.50 V), showing that the energetic favorability (Eq. 3.5) of reduction increases in this order.

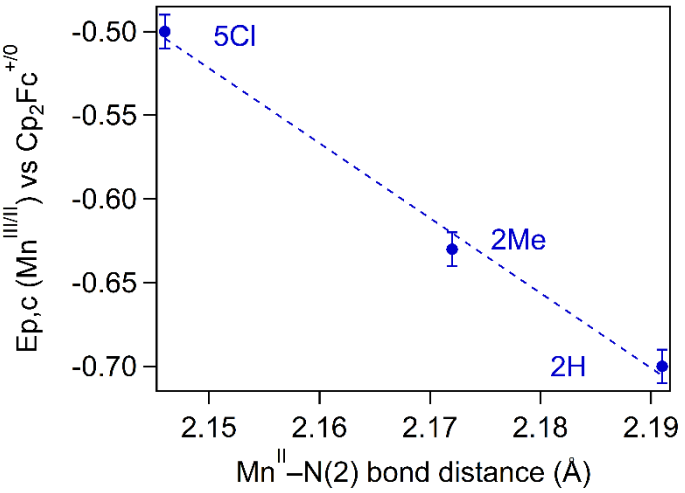

Figure 3.9 Experimental Ep,c ($Mn^{III/II}$) of $[Mn^{II}(OH_2)dpaq^{R}](OTf)$ complexes vs Mn^{II}–N(2) bond distances from X-ray diffraction data. The potentials are referenced to $Cp_2Fc^{+/0}$.

The behavior of plot of *Ep,c* ($Mn^{III/II}$) vs Mn^{II}–N(2) bond distances (Figure 3.9) suggests that this axial, amide nitrogen can modulate the effective electron affinity of the Mn^{III} center.

As described in chapter 2, our kinetic experiments were done in a 98:2 (vol:vol) $CH_3CN:H_2O$ solvent system and the BDFE analysis was done in a 90:10 (vol:vol) $CH_3CN:H_2O$ solvent system. In order to investigate the effect of higher amount of water in the solvent system, we compared the reactivity of $[Mn^{III}(OH)(dpaq^{5Cl})]OTf$ with TEMPOH in the above two solvent systems at -10 C°. Obtained second order rate constants are compared in Figure 3.20 and the ratio of k_2, at 98:2 (vol:vol) $CH_3CN:H_2O$: k_2, at 90:10 (vol:vol) $CH_3CN:H_2O$ in TEMPO–H reactivity at -10 °C is

4:1 (Figure 3.10). Generally the effect of changes in bulk properties such as polarity and viscosity that arise due to addition of a cosolvent are minimal in HAT reactivity.[16] However, water is an effective hydrogen bond donor and an acceptor. Therefore, water can affect the local environment in which the HAT reaction occurs causing changes in HAT reactivity.[17]

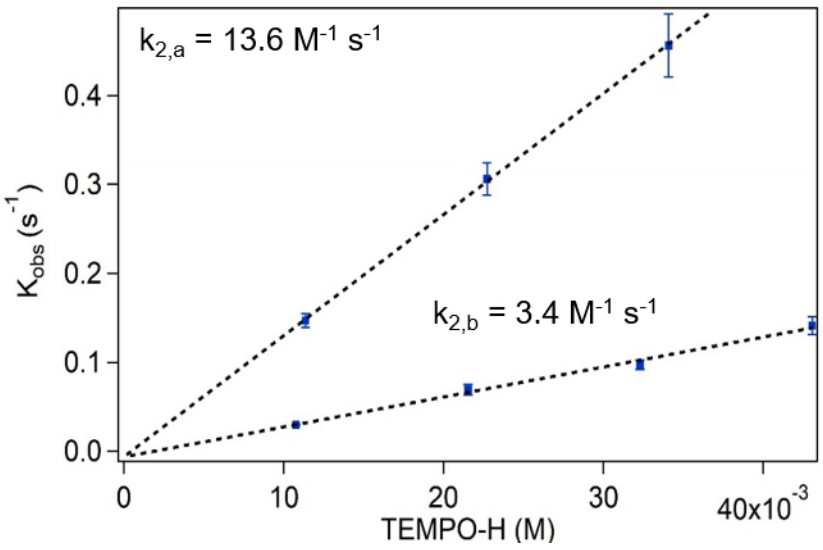

Figure 3.10 Second order rate constant comparison for the reaction between [Mn^{III}(OH)(dpaq^{5Cl})](OTf) with TMEPOH in 98:2 (vol:vol) CH_3CN:H_2O (k_2,a) solvent system and 90:10 (vol:vol) CH_3CN:H_2O solvent system (k_2,b) at -10 ˚C.

3.4 Conclusions

This study introduces the preparation of a series of [$Mn^{II}(OH_2)$(dpaq^{R})](OTf) (R = H, 2Me and 5Cl) complexes in a CH_3CN:H_2O solvent mixture. The $Mn^{III/II}$ reduction peak potentials shows a linear correlation with the distance between axial amide nitrogen and Mn^{III} in the above solvent system. The effect of additional water in the medium when changing solvents from in 98:2 (vol:vol) CH_3CN:H_2O to in 90:10 (vol:vol) CH_3CN:H_2O decreases the HAT reactivity by four folds.

3.5 References

1. Hynes, J. T., *Hydrogen-Transfer Reactions. Vol. 4: Biological aspects III - V*. WILEY-VCH: Weinheim, 2007; p 1207.

2. Mayer, J. M., Understanding Hydrogen Atom Transfer: From Bond Strengths to Marcus Theory. *Accounts of Chemical Research* **2011,** *44* (1), 36-46.

3. Wu, A.; Mayer, J. M., Hydrogen Atom Transfer Reactions of a Ruthenium Imidazole Complex: Hydrogen Tunneling and the Applicability of the Marcus Cross Relation. *Journal of the American Chemical Society* **2008,** *130* (44), 14745-14754.

4. Goldsmith, C. R.; Cole, A. P.; Stack, T. D. P., C−H Activation by a Mononuclear Manganese(III) Hydroxide Complex: Synthesis and Characterization of a Manganese-Lipoxygenase Mimic? *Journal of the American Chemical Society* **2005,** *127* (27), 9904-9912.

5. Coggins, M. K.; Brines, L. M.; Kovacs, J. A., Synthesis and Structural Characterization of a Series of MnIIIOR Complexes, Including a Water-Soluble MnIIIOH That Promotes Aerobic Hydrogen-Atom Transfer. *Inorganic Chemistry* **2013,** *52* (21), 12383-12393.

6. Porter, T. R.; Mayer, J. M., Radical reactivity of theFe(III)/Fe(II) tetramesitylporphyrin couple: hydrogen atom transfer, oxyl radical dissociation, and catalytic disproportionation of a hydroxylamine. *Chem. Sci.* **2014,** *5* (1), 372-380.

7. Larsen, A. S.; Wang, K.; Lockwood, M. A.; Rice, G. L.; Won, T.-J.; Lovell, S.; Sadílek, M.; Tureček, F.; Mayer, J. M., Hydrocarbon Oxidation by Bis-μ-oxo Manganese Dimers: Electron Transfer, Hydride Transfer, and Hydrogen Atom Transfer Mechanisms. *Journal of the American Chemical Society* **2002,** *124* (34), 10112-10123.

8. Puri, M.; Que, L., Toward the Synthesis of More Reactive S = 2 Non-Heme Oxoiron(IV) Complexes. *Accounts of Chemical Research* **2015,** *48* (8), 2443-2452.

9. Rice, D. B.; Massie, A. A.; Jackson, T. A., Manganese–Oxygen Intermediates in O–O Bond Activation and Hydrogen-Atom Transfer Reactions. *Accounts of Chemical Research* **2017,** *50* (11), 2706-2717.

10. Massie, A. A.; Sinha, A.; Parham, J. D.; Nordlander, E.; Jackson, T. A., Relationship between Hydrogen-Atom Transfer Driving Force and Reaction Rates for an Oxomanganese(IV) Adduct. *Inorganic Chemistry* **2018,** *57* (14), 8253-8263.

11. Matsuo, T.; Mayer, J. M., Oxidations of NADH Analogues bycis-[RuIV(bpy)2(py)(O)]2+Occur by Hydrogen-Atom Transfer Rather than by Hydride Transfer. *Inorganic Chemistry* **2005,** *44* (7), 2150-2158.

12. Warren, J. J.; Tronic, T. A.; Mayer, J. M., Thermochemistry of Proton-Coupled Electron Transfer Reagents and its Implications. *Chemical Reviews* **2010,** *110* (12), 6961-7001.

13. Klein, J. E. M. N.; Dereli, B.; Que, L.; Cramer, C. J., Why metal–oxos react with dihydroanthracene and cyclohexadiene at comparable rates, despite having different C–H bond strengths. A computational study. *Chemical Communications* **2016,** *52* (69), 10509-10512.

14. Rice, D. B.; Wijeratne, G. B.; Burr, A. D.; Parham, J. D.; Day, V. W.; Jackson, T. A., Steric and Electronic Influence on Proton-Coupled Electron-Transfer Reactivity of a Mononuclear Mn(III)-Hydroxo Complex. *Inorganic Chemistry* **2016,** *55* (16), 8110-8120.

15. Pavlishchuk, V. V.; Addison, A. W., Conversion constants for redox potentials measured versus different reference electrodes in acetonitrile solutions at 25°C. *Inorganica Chimica Acta* **2000,** *298* (1), 97-102.

16. Avila, D. V.; Brown, C. E.; Ingold, K. U.; Lusztyk, J., Solvent effects on the competitive .beta.-scission and hydrogen atom abstraction reactions of the cumyloxyl radical. Resolution of a long-standing problem. *Journal of the American Chemical Society* **1993,** *115* (2), 466-470.

17. Warren, J. J.; Mayer, J. M., Tuning of the Thermochemical and Kinetic Properties of Ascorbate by Its Local Environment: Solution Chemistry and Biochemical Implications. *Journal of the American Chemical Society* **2010,** *132* (22), 7784-7793.

Appendix 1

Table A1 1 Crystal data and structure refinement for [Mn(N5C23H19CLO)(O3SCF3)].

Identification code	q34h	
Empirical formula	C24 H19 Cl F3 Mn N5 O4 S	
Formula weight	620.89	
Temperature	200(2) K	
Wavelength	1.54178 Å	
Crystal system	Triclinic	
Space group	P-1	
Unit cell dimensions	a = 9.3685(2) Å	□= 94.4199(6)°.
	b = 9.4125(2) Å	□= 105.5681(7)°.
	c = 16.6418(3) Å	□ = 112.8309(7)°.
Volume	1275.47(5) $Å^3$	
Z	2	
Density (calculated)	1.617 Mg/m^3	
Absorption coefficient	6.516 mm^{-1}	
F(000)	630	
Crystal size	0.125 x 0.070 x 0.050 mm^3	
Theta range for data collection	2.816 to 70.334°.	
Index ranges	-10<=h<=9, -11<=k<=11, -20<=l<=20	
Reflections collected	16700	
Independent reflections	4487 [R(int) = 0.0339]	
Completeness to theta = 66.000°	95.5 %	
Absorption correction	Multi-scan	
Max. and min. transmission	1.000 and 0.761	
Refinement method	Full-matrix least-squares on F^2	
Data / restraints / parameters	4487 / 0 / 353	
Goodness-of-fit on F^2	1.078	
Final R indices [I>2sigma(I)]	R1 = 0.0483, wR2 = 0.1192	
R indices (all data)	R1 = 0.0500, wR2 = 0.1207	
Extinction coefficient	0.0088(7)	
Largest diff. peak and hole	0.801 and -0.951 $e.Å^{-3}$	

Table A.1.2 Atomic coordinates ($\times 10^4$) and equivalent isotropic displacement parameters ($Å^2 \times 10^3$)
for [Mn(N5C23H19CLO)(O3SCF3)]. U(eq) is defined as one third of the trace of the orthogonalized U^{ij} tensor.

	x	y	z	U(eq)
Mn	3486(1)	1237(1)	2546(1)	25(1)
Cl	10055(1)	4828(1)	6443(1)	48(1)
O(1)	4962(3)	-2122(2)	3599(2)	40(1)
N(1)	5195(3)	3204(3)	3672(1)	30(1)
N(2)	4632(3)	174(2)	3448(1)	26(1)
N(3)	2308(3)	-1361(3)	1809(1)	29(1)
N(4)	5107(3)	1161(3)	1775(2)	34(1)
N(5)	935(3)	166(3)	2607(2)	35(1)
C(1)	5404(4)	4690(3)	3758(2)	39(1)
C(2)	6644(5)	5883(4)	4436(2)	47(1)
C(3)	7676(4)	5511(3)	5028(2)	41(1)
C(4)	7477(3)	3942(3)	4977(2)	30(1)
C(5)	8465(3)	3442(3)	5574(2)	32(1)
C(6)	8191(4)	1897(4)	5488(2)	36(1)
C(7)	6918(4)	761(3)	4796(2)	31(1)
C(8)	5916(3)	1166(3)	4171(2)	25(1)
C(9)	6192(3)	2793(3)	4273(2)	25(1)
C(10)	4285(3)	-1351(3)	3228(2)	28(1)
C(11)	2813(4)	-2263(3)	2431(2)	35(1)
C(12)	2917(4)	-1411(4)	1081(2)	39(1)
C(13)	4674(4)	-231(3)	1287(2)	34(1)
C(14)	5749(4)	-536(4)	941(2)	43(1)
C(15)	7298(4)	644(5)	1095(2)	50(1)
C(16)	7741(4)	2081(5)	1586(2)	52(1)
C(17)	6615(4)	2293(4)	1921(2)	45(1)
C(18)	514(3)	-1929(3)	1508(2)	36(1)
C(19)	-52(3)	-1306(4)	2163(2)	34(1)
C(20)	-1544(4)	-2177(5)	2272(2)	48(1)
C(21)	-2054(5)	-1500(6)	2833(3)	59(1)
C(22)	-1072(6)	10(6)	3272(3)	62(1)
C(23)	415(5)	808(5)	3150(2)	50(1)

S	1991(1)	3029(1)	1123(1)	46(1)
F(11)	2875(4)	4413(4)	-78(2)	104(1)
F(12)	4469(3)	5570(3)	1149(2)	69(1)
F(13)	4505(7)	3515(5)	612(3)	131(2)
O(11)	2968(3)	3077(3)	1966(1)	41(1)
O(12)	1208(7)	1514(4)	600(2)	132(2)
O(13)	1039(4)	3895(6)	1103(3)	102(2)
C(24)	3535(4)	4179(4)	680(2)	43(1)

Table A1.3 Crystal data and structure refinement for [Mn^{III}(OH)(dpaq^{5Cl})](OTf).

Identification code	q70g	
Empirical formula	C26 H23 Cl F3 Mn N6 O5 S	
Formula weight	678.95	
Temperature	200(2) K	
Wavelength	1.54178 Å	
Crystal system	Monoclinic	
Space group	P21/n	
Unit cell dimensions	a = 9.2731(2) Å	α = 90°.
	b = 24.9494(5) Å	β = 96.7746(10)°.
	c = 12.5251(2) Å	γ = 90°.
Volume	2877.55(10) Å3	
Z	4	
Density (calculated)	1.567 Mg/m3	
Absorption coefficient	5.868 mm-1	
F(000)	1384	
Crystal size	0.180 x 0.170 x 0.075 mm3	
Theta range for data collection	3.543 to 70.193°.	
Index ranges	-9<=h<=11, -30<=k<=30, -14<=l<=15	
Reflections collected	32798	
Independent reflections	5367 [R(int) = 0.0577]	
Completeness to theta = 66.000°	99.9 %	
Absorption correction	Multi-scan	
Max. and min. transmission	1.000 and 0.623	
Refinement method	Full-matrix least-squares on F2	
Data / restraints / parameters	5367 / 19 / 427	
Goodness-of-fit on F2	1.052	
Final R indices [I>2sigma(I)]	R1 = 0.0445, wR2 = 0.1101	
R indices (all data)	R1 = 0.0490, wR2 = 0.1145	
Extinction coefficient	0.00153(16)	
Largest diff. peak and hole	1.013 and -0.404 e.Å-3	

Table A1.4 Atomic coordinates ($\times 0^4$) and equivalent isotropic displacement parameters ($Å^2 \times 10^3$)
for [Mn(OH)(C23H19ClN5O)][O3SCF3]-CH3CN. U(eq) is defined as one third of the trace of the orthogonalized U^{ij} tensor.

	x	y	z	U(eq)
Mn	4984(1)	1983(1)	1201(1)	25(1)
Cl	2768(1)	54(1)	4607(1)	80(1)
O(1)	4343(2)	2039(1)	-214(1)	38(1)
O(2)	7026(2)	2286(1)	4200(1)	42(1)
N(1)	3946(2)	1279(1)	1526(2)	29(1)
N(2)	5661(2)	1900(1)	2748(2)	27(1)
N(3)	6290(2)	2704(1)	1384(2)	29(1)
N(4)	3442(2)	2594(1)	1737(2)	32(1)
N(5)	7108(2)	1727(1)	726(2)	34(1)
C(1)	3128(3)	976(1)	828(2)	38(1)
C(2)	2375(3)	529(1)	1153(3)	47(1)
C(3)	2487(3)	397(1)	2214(3)	45(1)
C(4)	3376(3)	704(1)	2980(2)	37(1)
C(5)	3616(3)	606(1)	4093(2)	48(1)
C(6)	4506(4)	925(1)	4767(2)	52(1)
C(7)	5235(3)	1365(1)	4371(2)	40(1)
C(8)	5049(2)	1484(1)	3287(2)	28(1)
C(9)	4107(2)	1148(1)	2596(2)	28(1)
C(10)	6571(2)	2270(1)	3236(2)	28(1)
C(11)	7073(3)	2694(1)	2494(2)	35(1)
C(12)	5303(3)	3172(1)	1192(2)	38(1)
C(13)	3951(3)	3098(1)	1724(2)	34(1)
C(14)	3238(3)	3524(1)	2142(2)	49(1)
C(15)	1982(3)	3424(2)	2602(3)	60(1)
C(16)	1470(3)	2905(2)	2636(3)	56(1)
C(17)	2224(3)	2499(1)	2185(2)	43(1)
C(18)	7315(3)	2688(1)	562(2)	38(1)
C(19)	7945(3)	2136(1)	479(2)	35(1)
C(20)	9271(3)	2055(1)	102(2)	47(1)
C(21)	9728(4)	1539(2)	-39(3)	59(1)
C(22)	8882(4)	1118(1)	214(3)	58(1)

C(23)	7584(3)	1225(1)	606(2)	45(1)
S	8434(1)	-479(1)	2090(1)	36(1)
F(11)	5920(3)	-181(2)	1095(2)	73(1)
F(12)	5787(3)	-515(2)	2651(2)	88(1)
F(13)	6606(3)	273(1)	2492(2)	81(1)
O(11)	9024(6)	-459(2)	3203(3)	66(2)
O(12)	9065(5)	-118(2)	1392(4)	74(1)
O(13)	8181(5)	-1005(1)	1668(4)	63(1)
C(24)	6585(4)	-217(2)	2074(3)	49(1)
S'	8380(20)	-531(11)	2000(20)	110(11)
F(11')	5710(20)	-472(11)	1311(18)	69(7)
F(12')	6210(30)	-888(10)	2794(19)	74(8)
F(13')	6250(20)	-28(9)	2818(18)	59(7)
O(11')	9220(40)	-438(19)	3030(20)	30(7)
O(12')	8710(40)	-178(14)	1170(30)	58(11)
O(13')	8330(40)	-1089(11)	1720(30)	37(9)
C(24')	6500(20)	-451(10)	2239(19)	58(13)
N(1S)	10015(5)	1636(2)	3059(3)	92(1)
C(1S)	9678(4)	1269(1)	3491(3)	58(1)
C(2S)	9250(6)	810(2)	4097(4)	87(1)

Table A1.5 Crystal data and structure refinement for $[Mn^{III}Mn^{III}(\mu\text{-}O)(dpaq^{5Cl})_2](OTf)_2$.

Identification code	q54h	
Empirical formula	C50.80 H38 Cl2 F6 Mn2 N11.40 O9 S2	
Formula weight	1311.05	
Temperature	200(2) K	
Wavelength	1.54178 Å	
Crystal system	Monoclinic	
Space group	$P2_1/n$	
Unit cell dimensions	a = 22.5110(4) Å	α = 90°.
	b = 11.9178(2) Å	β = 122.9220(10)°
	c = 24.3401(4) Å	γ = 90°.
Volume	5481.35(17) $Å^3$	
Z	4	
Density (calculated)	1.589 Mg/m^3	
Absorption coefficient	6.123 mm^{-1}	
F(000)	2658	
Crystal size	0.185 x 0.055 x 0.010 mm^3	
Theta range for data collection	2.156 to 70.507°.	
Index ranges	-16<=h<=27, -14<=k<=14, -29<=l<=28	
Reflections collected	54994	
Independent reflections	10108 [R(int) = 0.0810]	
Completeness to theta = 66.000°	98.4 %	
Absorption correction	Multi-scan	
Max. and min. transmission	1.000 and 0.625	
Refinement method	Full-matrix least-squares on F^2	
Data / restraints / parameters	10108 / 60 / 745	
Goodness-of-fit on F^2	1.014	
Final R indices [I>2sigma(I)]	R1 = 0.0698, wR2 = 0.1863	
R indices (all data)	R1 = 0.0890, wR2 = 0.2057	
Extinction coefficient	n/a	
Largest diff. peak and hole	1.030 and -1.098 $e.Å^{-3}$	

Table A1.6 Atomic coordinates ($\times 10^4$) and equivalent isotropic displacement parameters ($Å^2 \times 10^3$) for [Mn(N5C23H19CLO)(O3SCF3)]. U(eq) is defined as one third of the trace of the orthogonalized U^{ij} tensor.

x	y	z	U(eq)	
Mn	3486(1)	1237(1)	2546(1)	25(1)
Cl	10055(1)	4828(1)	6443(1)	48(1)
O(1)	4962(3)	-2122(2)	3599(2)	40(1)
N(1)	5195(3)	3204(3)	3672(1)	30(1)
N(2)	4632(3)	174(2)	3448(1)	26(1)
N(3)	2308(3)	-1361(3)	1809(1)	29(1)
N(4)	5107(3)	1161(3)	1775(2)	34(1)
N(5)	935(3)	166(3)	2607(2)	35(1)
C(1)	5404(4)	4690(3)	3758(2)	39(1)
C(2)	6644(5)	5883(4)	4436(2)	47(1)
C(3)	7676(4)	5511(3)	5028(2)	41(1)
C(4)	7477(3)	3942(3)	4977(2)	30(1)
C(5)	8465(3)	3442(3)	5574(2)	32(1)
C(6)	8191(4)	1897(4)	5488(2)	36(1)
C(7)	6918(4)	761(3)	4796(2)	31(1)
C(8)	5916(3)	1166(3)	4171(2)	25(1)
C(9)	6192(3)	2793(3)	4273(2)	25(1)
C(10)	4285(3)	-1351(3)	3228(2)	28(1)
C(11)	2813(4)	-2263(3)	2431(2)	35(1)
C(12)	2917(4)	-1411(4)	1081(2)	39(1)
C(13)	4674(4)	-231(3)	1287(2)	34(1)
C(14)	5749(4)	-536(4)	941(2)	43(1)
C(15)	7298(4)	644(5)	1095(2)	50(1)
C(16)	7741(4)	2081(5)	1586(2)	52(1)
C(17)	6615(4)	2293(4)	1921(2)	45(1)
C(18)	514(3)	-1929(3)	1508(2)	36(1)
C(19)	-52(3)	-1306(4)	2163(2)	34(1)
C(20)	-1544(4)	-2177(5)	2272(2)	48(1)
C(21)	-2054(5)	-1500(6)	2833(3)	59(1)
C(22)	-1072(6)	10(6)	3272(3)	62(1)
C(23)	415(5)	808(5)	3150(2)	50(1)
S	1991(1)	3029(1)	1123(1)	46(1)

F(11)	2875(4)	4413(4)	-78(2)	104(1)
F(12)	4469(3)	5570(3)	1149(2)	69(1)
F(13)	4505(7)	3515(5)	612(3)	131(2)
O(11)	2968(3)	3077(3)	1966(1)	41(1)
O(12)	1208(7)	1514(4)	600(2)	132(2)
O(13)	1039(4)	3895(6)	1103(3)	102(2)
C(24)	3535(4)	4179(4)	680(2)	43(1)

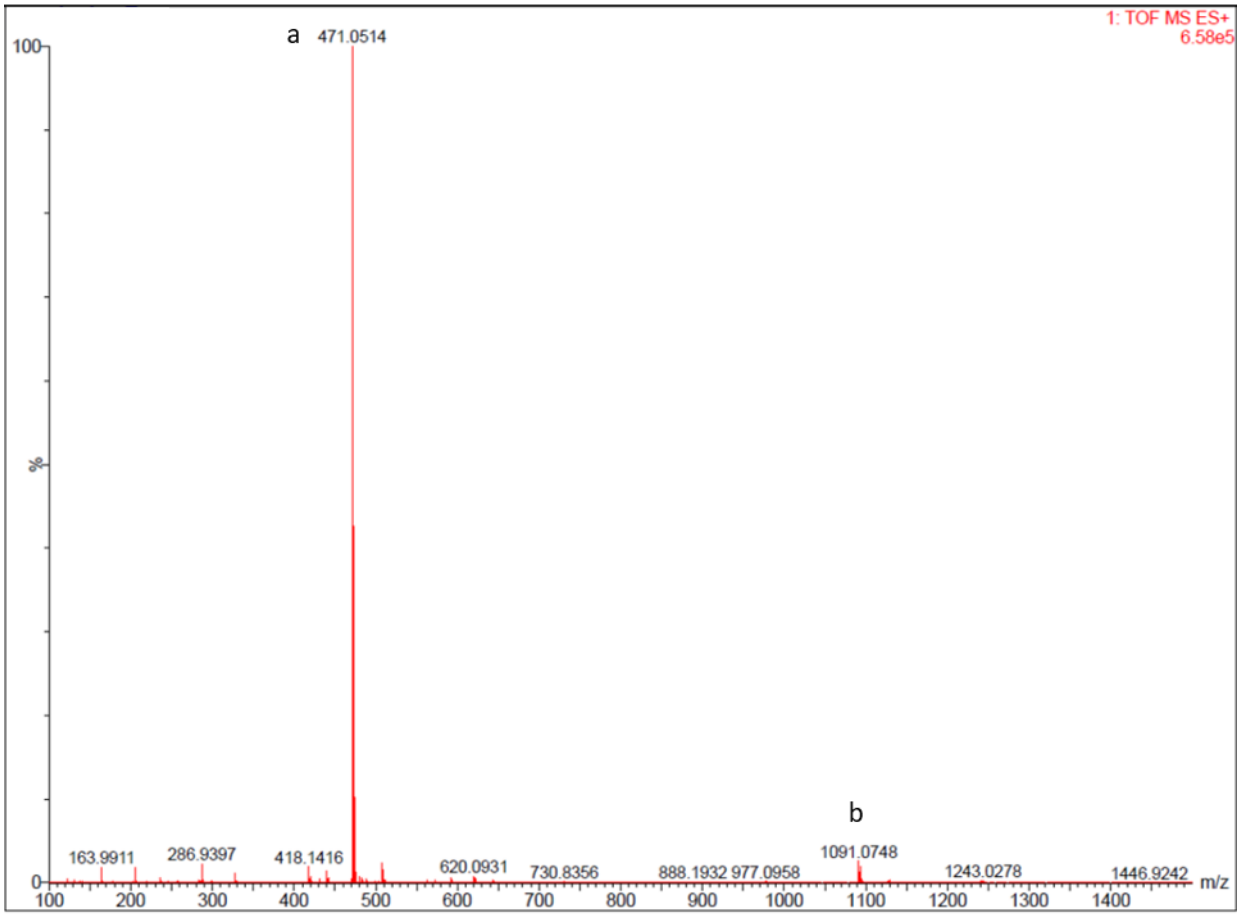

Figure A1.1 ESI-MS spectrum of $[Mn^{II}(dpaq^{5Cl})(OTf)]$ dissolved in CH_3CN. Peak assignments are as follows: a) $[Mn^{II}(dpaq^{5Cl})]^+$, c) $[Mn_2^{II}(dpaq^{5Cl})_2(OTf)]^+$.

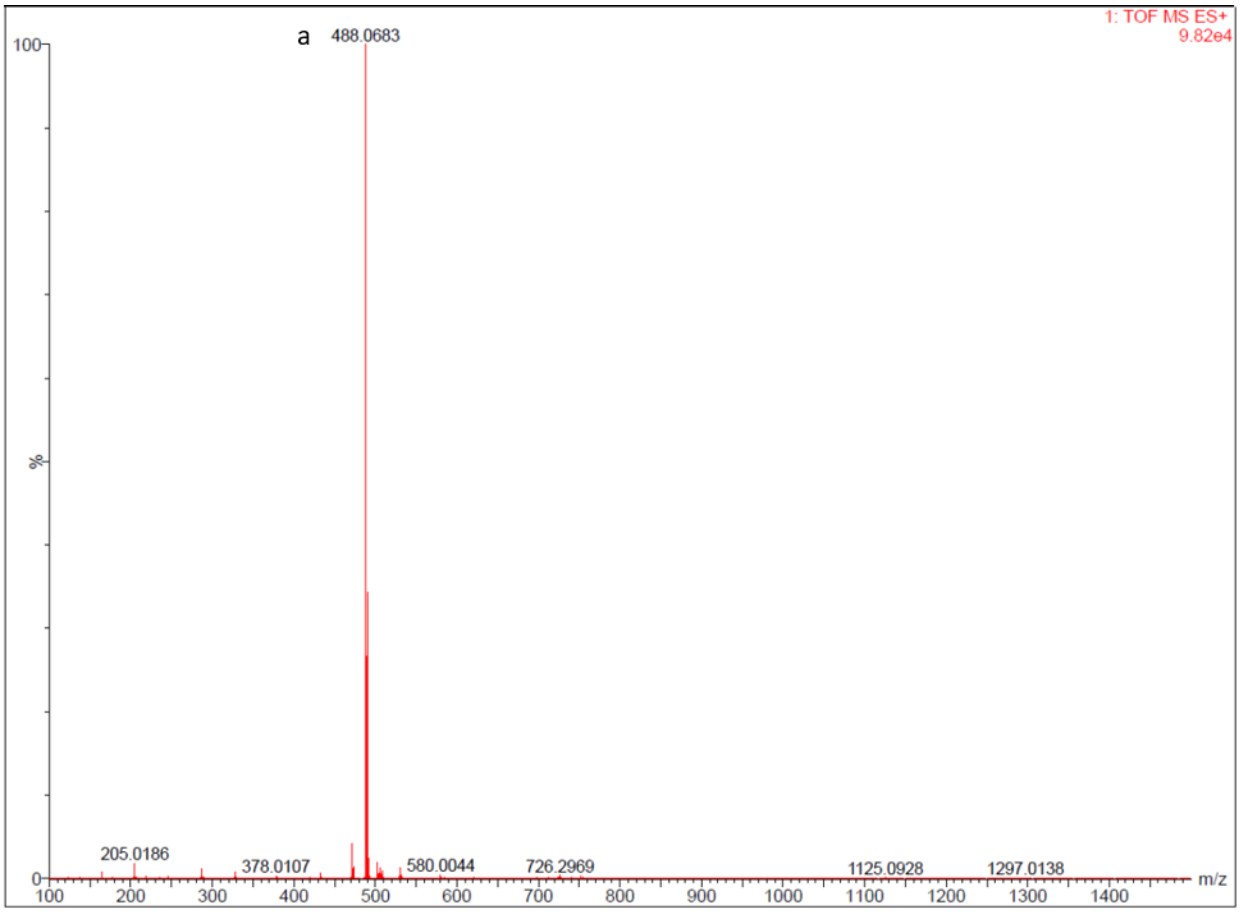

Figure A1.2 ESI-MS spectrum of $[Mn^{III}(OH)(dpaq^{5Cl})](OTf)$ dissolved in CH_3CN. Peak assignment: a) $[Mn^{III}(OH)(dpaq^{5Cl})]^+$.

Solid State Magnetic moment measurements

Method: Gouy method with a magnetic susceptibility balance

$$X_m = C_{Bal} \times l \times \frac{(R - R_0)}{10^9 \times m}$$

Where,

X_m : mass susceptibility

C_{Bal}: Calibration constant of the balance

R : balance reading for the sample in tube

R_0 : balance reading for empty tube

m : mass of sample in g

l : length of sample in cm

Parameter or Constant	Value
X_m	6.04 x 10^{-7} cm^3/g
C_{Bal}	1.103
R	-8.67
R_0	-31
m	0.0204 g
l	0.5 cm
MW	1311 g mol^{-1}

Diamagnetic contribution

Atom/bond	No. of atoms/bonds (N)	$X_{Di}/(1 \times 10^{-6}\ cm^3\ mol^{-1})$	$X_{Di}/(1 \times 10^{-6}\ cm^3\ mol^{-1})$*N
C(Ring)	19	-6.24	-118.56
C(open chain)	4	-6	-24
N(Ring)	3	-4.61	-13.83
N(open chain)	2	-5.57	-11.14
H	18	-2.93	-52.74
O	2	-4.6	-9.2
Mn	1	-10	-10
Cl	1	-20.1	-20.1
C-C	13	0	0
C=C	8	5.5	44
C-H	18	0	0
C-Cl	1	3.1	3.1
C=O	1	6.3	6.3
O-H	1	0	0
C-N	8	0	0
C=N	3	8.15	24.45
Mn-N	5	0	0
Mn-O	1	0	0
Total			-1.8×10^{-4}

Data for diamagnetic correction was obtained from ref. [1].

Calculation of μ_{eff}.

$$X_M = X_m \times \frac{MW}{2}$$

X_M = 0.000396

$X_M^{corr} = X_M^{exp} - X_M^{diam}$

X_M^{corr} = 0.000580

$$\mu_{eff} = \sqrt{\frac{3kTX_M^{corr}}{N_A\beta^2}} = 2.828\sqrt{X_M^{corr} \times T}$$

μ_{eff} = 1.18 μ_B per Mn

References

1. Bain, G. A.; Berry, J. F., Diamagnetic Corrections and Pascal's Constants. *Journal of Chemical Education* **2008,** *85* (4).